Universidade de Lisboa

Faculdade de Ciências

Departamento de Física

# U

## LISBOA

### UNIVERSIDADE
### DE LISBOA

# Advanced Brain Imaging: From Adult to Neonates

Rui Pedro Azeredo Gomes Teixeira

DISSERTAÇÃO

MESTRADO INTEGRADO EM ENGENHARIA BIOMÉDICA E BIOFÍSICA
PERFIL EM RADIAÇÕES EM DIAGNÓSTICO E TERAPIA

2013

Universidade de Lisboa

Faculdade de Ciências

Departamento de Física

# Advanced Brain Imaging: From Adult to Neonates

Rui Pedro Azeredo Gomes Teixeira

DISSERTAÇÃO

MESTRADO INTEGRADO EM ENGENHARIA BIOMÉDICA E BIOFÍSICA
PERFIL EM RADIAÇÕES EM DIAGNÓSTICO E TERAPIA

**Orientador Externo:**  Professor Doutor Joseph V. Hajnal
**Orientador Interno:**  Professora Doutora Rita G. Nunes

2013

# Resumo

Com o crescente aumento das intensidades de campo magnético e performance dos gradientes em ressonância magnética (RM), novas técnicas de imagiologia médica têm surgido que apresentam novos contrastes entre diferentes tecidos. No entanto, este tipo de imagens são desenvolvidas e optimizadas para o cérebro adulto que se sabe ter tempos de relaxação diferentes daqueles presentes no cérebro de um recém-nascido. Esta diferença é inerente ao alto teor em água presente no cérebro de um recém-nascido. O principal objectivo deste projecto é então proceder à optimização de técnicas avançadas de RM como susceptibilidade magnética (SWI) e de quantificação dos tempo de relaxação (DESPOT1 e DESPOT2) para o cérebro de recém-nascidos.

O sinal de RM é medido sob a forma de um número complexo caracterizado por uma intensidade e uma fase. Normalmente em RM, o sinal de fase é ignorado e apenas a intensidade do sinal é utilizada para proceder à reconstrução das imagens. No entanto, a fase do sinal complexo é extremamente rica em informação relativa às diferenças de susceptibilidade entre tecidos diferentes, sendo por isso bastante útil para realçar este tipo de contraste. Uma das questões que dificulta a utilização das imagens de fase é o facto de apenas poderem registar valores no intervalo de $[-\pi, \pi)$ o que resulta no mapeamento de valores que caiam fora desse intervalo para o seu interior. Uma vez que a informação de interesse nas imagens de fase corresponde a estruturas de pequena dimensão, caracterizadas por frequências elevadas no espaço de Fourier, SWI consiste na utilização de imagens de fase sujeitas a um filtro passa-alto simples (janela rectangular. Tal permite extraír a informação de interesse, que posteriormente é utilizada para realçar contraste de susceptibilidade em imagens de intensidade. Este mapeamento da informação de susceptibilidade na imagem de intensidade é realizado através da multiplicação da mesma por uma máscara extraída da imagem de fase filtrada para as baixas frequências. Isto tem um particular interesse para a visualização do sistema vascular venoso uma vez que diferenças de susceptibilidade entre sangue venoso e os tecidos envolventes permitem identificar estruturas venosas mesmo em vasos com dimensões inferiores à resolução de aquisição. Isto é possivel graças às propriedades paramagnéticas da deox-

ihemoglobina presente no sangue venoso. Neste trabalho o protocolo normalmente utilizado para SWI foi adpatado e implementado à realidade dos recém-nascidos. Ao mesmo tempo foi também desenvolvida uma interface gráfica de modo a facilitar o processamento e construção de imagens ponderadas em susceptibilidade. Este processamento foi desenvolvido integrando a FSL-FMRIB Software Library 5.0 juntamente com MatLab2012a. A interface gráfica foi desenvolvida em ambiente de programação MatLab2012a com o auxílio da ferramenta *guide*. Uma pequena discussão sobre o efeito da dimensão do voxel de aquisiọ também é incluída neste trabalho. É prática comum os voxeis das imagens de SWI serem adquiridos com um quociente entre a resolução do plano de visualização e a espessura dos cortes (AR, do inglês voxel *aspect ratio*) apresentar valores entre 2 e 4. No entanto, este tipo de aquisiọ induz uma excelente visualização apenas para um dos (normalmente o plano transversal) e uma muito má visualização nos restantes planos. Com isto em mente, resolveu-se também neste projecto, propôr a utilização de um voxel de aquisição isotrópico em detrimento do que é prática comum na literatura. Espera-se que este tipo de aquisição isotrópica reduza um pouco o contraste de susceptibilidade obtido, no entanto após inspeção visual de algumas imagens obtidas em voluntários decidimos que o ganho em informação nos dois restantes planos de visualização ortogonais justificaria essa pequena perda de contraste. Este facto não foi no entanto devidamente avaliado e mais estudos seriam necessários para uma correcta avaliação desta caracterítica.

Na segunda parte do projecto apresentado nesta tese, foi implementada uma técnica de quantificação em RM conhecida por *"Driven Equilibrium Single Pulse Observation of T1 and T2 - DESPOT1 e DESPOT2"*. Esta técnica (neste trabalho referida como DESPOT) permite de forma bastante rápida estimar $T_1$ e $T_2$. Mais uma vez, devido ao facto de o cérebro de recém-nascidos ter um conteúdo superior em água relativamente ao cérebro adulto, uma adaptação deve ser feita de modo a garantir a qualidade das imagens obtidas. Esta técnica consiste na utilização de sequências de RM conhecidas como *Steady-State Free Precession* (SSFP) e *Spoiled Gradient Echo* (SPGR) para obter imagens mantendo todos os parâmetros constantes, ao mesmo tempo que se variam os *Flip Angles* (FA). Isto permite ajustar um modelo matemático que melhor explique as medições realizadas de modo a estimar os tempos de relaxação $T_1$ e $T_2$. Para garantir a precisão da estimação dos parâmetros $T_1$ e $T_2$, simulações de Monte Carlo foram criadas onde se verificou que, usando a ferramenta de MatLab2012a *fminsearch*, como algoritmo de optimização é possível obter uma precisão de estimação (quociente entre variância de estimação e o quadrado do valor correcto) de aproximadamente 5% relativamente ao valor correcto. Uma avaliação da capacidade de estimar $T_1$ e $T_2$ foi realizada com modelos matemáticos de um e dois compartimentos que procuram explicar o sinal de RM medido em DESPOT. O modelo

de dois compartimentos foi publicado por Deoni et al. em 2008, onde foi sugerido que é possível estimar as fracções relativas de cada um dos compartimentos em cada voxel medido. No entanto, os resultados obtidos para o modelo de dois compartimentos não foram satisfatórios. Foi decidido que uma avaliação mais profunda e tentativa de resolução deste problema saía fora dos objectivos do projecto.

O *Crámer-Rao lower bound* (CRLB) (em português limite inferior de Crámer-Rao), é uma ferramenta estatística que permite estimar qual a variância miníma alcançável aquando da estimação de parâmetros com base no ajuste de um modelo matemático a um conjunto de medições. De modo a finalizar o trabalho apresentado nesta tese, proposémo-nos a utilizar a minimização do CRLB para seleccionar o conjunto de FA que permite estimar $T_1$ e $T_2$ com melhor precisão. Em primeiro lugar mostramos que a variância prevista pelo CRLB se encontra em concordância com a variância obtida com as simulações de Monte Carlo. Isto permite confirmar a viabilidade da utilização do CRLB para optimizar o protocolo de estimação de $T_1$ e $T_2$. Para tal, foi desenvolvida uma função de custo utilizando o CRLB para optimizar o conjunto de FA que minimiza e garante a melhor precisão considerando de uma matriz de combinações de $T_1$ e $T_2$. A função de custo consiste em minimizar o maior valor de precisão (definida como o quociente entre a variância e o quadrado do valor correcto para o parâmetro) é calculada numa grelha de combinações de parâmetros $T_1$ e $T_2$, garantindo assim, que a cada iteração do processo de optimização o pior cenário era minimizado. Os resultados obtidos permitiram concluir que é possível optimizar o protocolo de DESPOT garantindo uma precisão minima num grelha de combinções de diferentes $T_1$ e $T_2$. Foi também possível concluir que se pode reduzir significativamente o número de medições necessárias para a estimação sem aumentar significativamente a precisão desta. Este facto é de extrema importância para obter imagens de RM em recém nascidos onde é necessário reduzir o tanto quanto possível os tempos de aquisição de modo evitar artefactos de movimento.

Ambas as vertentes (SWI e DESPOT) deste projecto foram avaliadas pela equipa técnica e estão aptas a serem incorporadas em ambiente clínico permitindo o desenvolvimento de futuros projectos nestas áreas.

**Palavras-Chave:** MRI, Optimização, Estimação, SWI, DESPOT

# Abstract

With recent increase of clinical MR field strength and gradient performance, advanced imaging techniques have been proposed that allow new types of contrast and tissue parameter quantification. However this advanced techniques are typically optimized to the adult brain which is known to have different relaxation times $T_1$ and $T_2$ relative to the neonatal brain because of its higher water content. The main purpose of this work is to optimize advanced imaging techniques such as susceptibility weighted imaging (SWI) and driven equilibrium single pulse observation of $T_1$ and $T_2$ (DESPOT1 and DESPOT2) in order to be applied to the neonatal brain.

In this work, a neonatal SWI protocol was developed by adapting a gold standard adult protocol presented in the literature. Also a graphical user interface was developed in order to provide an easy tool to reconstruct susceptibility weighted images. Single compartment and multi-compartment DESPOT estimation precision was estimated from both a Monte Carlo (MC) and Cramer-Rao Lower Bound (CRLB) approaches. CRLB is a statistical tool that allows us to estimate the minimum possible variance that can be obtained when estimating parameters of a mathematical model given a set of independent noisy measurements. Furthermore, the CRLB was used as a tool to optimize the DESPOT protocol regarding both precision and acquisition time.

In this work a neonatal SWI protocol is proposed. Also we show that the CRLB can be used to optimize the DESPOT1 and DESPOT2 acquisition scheme and that the number of measurements usually made can be reduced without significantly compromising parameter estimation.

**Keywords:** MRI, Optimization, Estimation, SWI, DESPOT

# Acknowledgements

In this section of the thesis I want to thank everyone whom I feel to be important and that in some way or another helped me out during the realization of this project.

In first place I must thank my family who always supported me and encouraged me to take risks and go abroad in order to grow as human being, without their support I would have never been able to enrol in this project.

I must also thank my supervisors Jo and Rita who where amazing during my stay at the CDB, they have both always shown great interest and support during this project and I would have never been able to grow as much as I did as a scientist without them. Shaihan was not officially my supervisor, however he was essential in the support I received at the CDB, and therefore I'm really glad that I had the opportunity to work with him and learn from him. I am definitely grateful to both Jo and Shaihan for educating me into the scientific way of thinking.

All this however could never had been done without the support of my co-workers from rooms 6, specially Fran, Georgia and KB. Fran was definitely amazing during the entire project and has always given great advice in times of need. The coffe-breaks/discussions mid-afternoon sessions with Fran and Tomoki were really important for the good environment I felt in the office.

I must also be grateful to Serena, Joanna and Tomoki for always being extremely helpful when real-life data was needed. They were fundamental in the good environment I felt at the CDB.

The cake club really helped to sweeten my weeks, while the great moments shared with Arian, Giulio, Markus, Sally, Yolanda and Kirsten made me enjoy much more my stay in London.

# Contents

# List of Figures

# Chapter 1

# Overview

Magnetic resonance imaging (MRI) is nowadays widely used as a medical imaging approach by making use of interactions between some magnetic nuclei and applied external magnetic fields to produce images of the human body. As will be explained in section 2.1 each MR image voxel is recorded in the form of a complex number where magnitude and phase information reflect the interaction between specific nuclei and the applied magnetic fields.

On conventional MR techniques, often used in a clinical setting, phase information is discarded and only the magnitude image, composed of a mixture of contrasts caused by different tissue properties, is used to probe the desired information[1]. Advanced imaging techniques allow us to further improve the quality of information obtained from MR imaging, and to evaluate a larger range of tissue parameters. The ability to probe tissue specific properties such as magnetic susceptibility, and relaxation times $T_1$ and $T_2$, has been proven to be useful in detecting and understanding diseases [2, 3, 4].

Being able to quantify tissue properties is of special importance in the neonatal brain, because it opens a window of opportunity to study *in vivo* how the human brain matures with age. The main goal of this project is therefore to be able to adapt advanced imaging techniques such as Susceptibility Weighted Imaging (SWI) and Driven Equilibrium Single Pulse Observation of T1 and T2 (DESPOT), initially developed for adult imaging, to visualise the newborn brain and how it matures with age.

In chapter 2 a brief explanation of the background necessary to introduce the work presented within this thesis is shown.

Chapter 3 will focus on the development of a SWI neonatal protocol. This involved proposing a dedicated neonatal protocol, including a re-evalution of the effect of varying slice thickness, developing a graphical

user interface to allow users to produce filtered images that emphasise susceptibility effects from raw SWI data.

Within chapter 4 it is discussed how to correctly process a set of multi-angle SPGR and SSFP signals in order to estimateT1andT2for both a one compartment and two compartment model.

Chapter 5 focused in the use of the CRLB as an optimization tool for DESPOT.

# Chapter 2

# Background Material

Within this chapter, the basic principles of magnetic resonance imaging (MRI) necessary to understand the work presented in this thesis are presented.

As stated in [5] the idea of using spatial varying magnetic fields in order to obtain information about a given object was first proposed and demonstrated by Lauterbur and Mansfield in 1973. This moment in history may be considered as the birth of Magnetic Resonance Imaging (MRI) which quickly evolved into the technique which is is nowadays used in Hospital environment.

## 2.1 Basic Principles of MRI

The fundamental principals of MRI are based on the interaction between atomic nuclei and external magnetic fields. When subjected to a static magnetic field, some atomic nuclei present energy states with different energy levels, whose energy difference is proportional to the applied magnetic field [6]. This effect is known as the Zeeman effect [6], and is direct consequence of the atomic nuclei intrinsic angular momentum also known as Spin.

### 2.1.1 Larmor Frequency

Considering the case of a single proton, since it is a charged particle, its spin property can be related to a circulating electric current, and, therefore an associated magnetic moment [5]. The relationship between the magnetic momentum and the spin angular momentum is defined as shown in Equation 2.1.

$$\vec{\mu} = \gamma \vec{J} \tag{2.1}$$

In Equation 2.1 the proportionality constant $\gamma$ between the magnetic moment $\vec{\mu}$ and the spin angular moment $\vec{J}$ is called the gyromagnetic ratio and its value depends on the atomic nuclei under consideration[5]. The human body has a very high content of water and therefore the gyromagnetic ratio for the hydrogen nucleus which has a value $\gamma = 42.58$ MHz/T is a very important parameter in MRI. By combining Equation 2.1 with the expression for torque on a magnetic moment due to an external magnetic field $\vec{B_0}$, oriented along the $z$ axis, we obtain the relationship shown in Equation 2.2 which describes the rotation and precession movements of atomic nuclei.

$$\frac{d\vec{\mu}}{dt} = \gamma \vec{\mu} \times \vec{B_0} \tag{2.2}$$

Which can also be represented as,

$$\frac{d\mu_x}{dt} = \gamma \mu_y B_0 \tag{2.3}$$

$$\frac{d\mu_y}{dt} = -\gamma \mu_x B_0 \tag{2.4}$$

$$\frac{d\mu_z}{dt} = 0 \tag{2.5}$$

and by combining the first two equations gives,

$$\frac{d^2}{dt^2} \begin{pmatrix} \mu_x \\ \mu_y \end{pmatrix} + (\gamma B_0)^2 \begin{pmatrix} \mu_x \\ \mu_y \end{pmatrix} = 0 \tag{2.6}$$

which has the solution,

$$\vec{\mu} = \begin{pmatrix} \mu_{x0} \cos \omega t + \mu_{y0} \sin \omega t \\ \mu_{y0} \cos \omega t - \mu_{x0} \sin \omega t \end{pmatrix} \tag{2.7}$$

where,

$$\omega = \gamma B_0 \tag{2.8}$$

The quantity $\omega$ in equation 2.8 is known as the Larmor frequency and represents the resonance frequency at which the magnetic nuclei precess around the main magnetic field.[6] This frequency is also the basic principle behind all MR imaging methods as it allows us to discriminate the sample in frequency steps by applying a gradient field $B_0 + r.G$.[5, 6] For example if we were to select a single slice, located at position $z_0$, from a sample then, by adding a gradient $G_z$ to the main field, it is possible to discriminate different Larmor frequencies along the $z$ direction of the sample. Frequency discrimination is possible because only excitation pulses with

frequencies very similar to the Larmor frequency significantly interact with the precessing atomic nuclei.[6]

### 2.1.2  Free Induction Decay

When in the presence of a static magnetic field, due to the generated torque protons tend to align themselves with its direction, depending on their intrinsic spin, either along the parallel direction (low energy state) or the anti-parallel direction (high-energy state) (Figure 2.1). Through the inter-
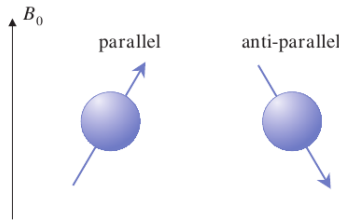


**Figure 2.1:** Two possible orientations for a proton when subjected to an external magnetic field. Adapted from [7]

action with applied excitation pulses (also known as RF pulses) it is possible to disturb this equilibrium state and flip the magnetic moments. The most common flip pulses are the $\pi/2$ pulse and the $\pi$ pulse that are responsible for flipping the magnetization vector by respectively 90° and 180°. Nevertheless it is possible to flip the magnetization moment by any angle by changing the RF pulse accordingly.[5]

When applying an $\pi/2$ pulse the magnetization vector which was oriented along the $B_0$ field flips towards the transverse plane $xy$ as shown in Figure 2.2. This new state is an excited state because the proton accumulated
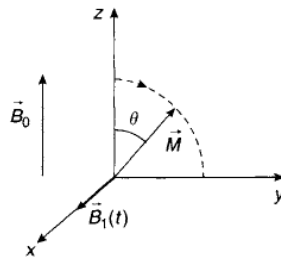


**Figure 2.2:** Representation of an excitation pulse in the rotating reference frame.The magnetization vector $M$ is initially aligned with $B_0$. An RF excitation pulse $B_1(t)$ is applied along the x axis resulting in the rotation to the $yz$ plane by the flip angle $\theta$. [8]

energy from the RF-pulse. However the protons tend to release its energy
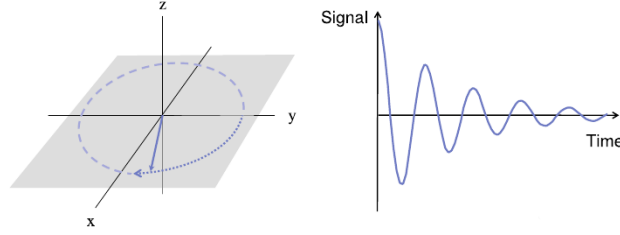
**Figure 2.3:** Precession of the flipped magnetization in the $M_{xy}$ plane (left) and the induced signal in the receiver coil (right)[7]

as a RF-pulse while decaying towards its resting state giving origin to the free induction decay (FID) signal as shown in Figure 2.3. This signal is modelled by the Bloch equations as explained in [5] and in [6]. This set of equations may be written as[6]:

$$\frac{dM_{x,y}}{dt} = \gamma(\vec{M} \times \vec{B_0})_{xy} - \frac{M_{x,y}}{T_2} \tag{2.9}$$

$$\frac{dM_z}{dt} = \gamma(\vec{M} \times \vec{B_0})_z - \frac{M_0 - M_z}{T_1} \tag{2.10}$$

where $T_2$ and $T_1$ are denominated, respectively, as the transverse and the longitudinal relaxation times, and $M_0$ is the equilibrium magnetization assumed to lie along the $z$ axis. The application of a $\pi/2$ pulse to the system along the transverse plane results in:

$$\frac{dM_x}{dt} = \gamma M_y B_0 - \frac{M_x}{T_2} \tag{2.11}$$

$$\frac{dM_y}{dt} = -\gamma M_x B_0 - \frac{M_y}{T_2} \tag{2.12}$$

with their respective solutions:

$$M_x(t) = M_0 e^{-\frac{t}{T_2}} \cos(\gamma B_0 t) \tag{2.13}$$

$$M_y(t) = -M_0 e^{-\frac{t}{T_2}} \sin(\gamma B_0 t) \tag{2.14}$$

from which we can extract the oscillating FID solution presented in Figure 2.3. We still need to consider the longitudinal solution of the Bloch equations. Since $\vec{B_0}$ lies entirely along the $z$ axis Equation 2.10 becomes:

$$\frac{dM_z}{dt} = \frac{M_0 - M_z}{T_1} \tag{2.15}$$

and by considering $M_z(0) = 0$ we obtain,

$$M_z(t) = M_0[1 - e^{-(\frac{t}{T_1})}] \tag{2.16}$$

6

which explains the longitudinal relaxation rate caused by "spin-lattice" interactions that induce the decay of the magnetization vector back to its resting state oriented along the $B_0$ field.[6] "Spin-spin" interactions result in another relaxation effect that must be taken into account in order to obtain a more realistic assessment of the MR signal. After the $\pi/2$ pulse applied at each time interval $T_R$, spins interact with each other causing local magnetic field variations and consequently, due to precessment movement differences, local Larmor frequencies changes arise.[5] This attenuation is modeled by $e^{-T_E/T_2}$, where $T_E$ is the instant at which the data is sampled, allowing us to obtain the following expression to describe the transverse magnetization evolution,

$$M_{x,y}(T_E) = M_0(1 - e^{-T_R/T_1})e^{-T_E/T_2} \qquad (2.17)$$

The $T_2$ effect does not account for field inhomogeneities which produce additional signal suppression. With this in mind it is of special importance to define a more global relaxation rate: the $T_2^*$ capable of taking into account external field induced effects ($T_2'$) and "spin-spin" interactions ($T_2$).[5]

$$\frac{1}{T_2^*} = \frac{1}{T_2} + \frac{1}{T_2'} \qquad (2.18)$$

As will be further explained in section 2.2.2, magnetic susceptibility directly relates to local magnetic field inhomogeneities. Taking these signal effects into account is of special importance since different local field inhomogeneities produce different levels of signal attenuation and dephasing, and therefore different levels of susceptibility contrast.

### 2.1.3 Frequency Encoding

As stated in section 2.1.1 the addition of a linear varying field to the main magnetic field allows us to create a linear space dependent Larmor frequency distribution as shown in Equation 2.19.

$$\omega_G(z, t) = \gamma z G(t) \qquad (2.19)$$

The use of a gradient to establish a relation as shown in 2.19, where the position of spins along a known direction results in a specific precessional distribution is referred to as frequency encoding along that direction[5].

For the one dimensional case (1D) Equation 2.19 allows us to measure the signal as being:

$$s(k) = \int \rho(z)\mathrm{e}^{-i2\pi kz}dz \qquad (2.20)$$

here, the time dependence is implicitly defined in the spatial frequency $k$ : $k(t) = \gamma \int_0^t dt' G(t')$.[5] Equation 2.20 is one of the main building blocks of

MR imaging reconstruction when linear gradients are applied. The measured signal $s(k)$ is the Fourier transform of the spin density of the sample and as a consequence the spin density can be determined by applying the inverse Fourier transform of the signal $s(k)$. [5]

$$\rho(z) = \int s(k)(e)^{+i2\pi kz} dk \tag{2.21}$$

### 2.1.4 Gradient Echo

Gradient echo sequences are of special interest in the measurement of $T_2^*$ effects since they are extremely sensitive to this relaxation rate. As stated in section 2.1.2, $T_2^*$ is strongly correlated with field inhomogeneities and therefore, by using acquisition sequences sensitive to this parameter it is possible to map local field variations. Haemoglobin (Hb) is an oxygen carrying molecule present in red blood cells, whose magnetic properties depend on the presence or absence of oxygen. Oxyhaemoglobin (oHb) is diamagnetic and Deoxyhaemoglobin (dHb) is paramagnetic, therefore local magnetic properties are modified by the oxygenation state allowing Susceptibility Weighted (SW) imaging to make use of gradient echo sequences to map local magnitude and phase changes that naturally occur in the human brain.[6] Thanks to dHb presence in venous blood vessels and bleeds, SW imaging is able to produce reliable venographic images of the human brain as well as detecting micro-bleeds inside it.

In a simple gradient echo sequence (Figure 2.4), an excitation pulse is applied (also known as RF-pulse), followed by a gradient field which is superimposed with $B_0$. The RF-pulse causes the magnetization to flip towards the $xy$ plane. Nuclei found in more intense fields start precessing at larger frequencies compared to the ones found in weaker fields resulting in spin dephasing. The applied gradient is then reversed at a later time allowing the "*fast*" nuclei to be placed in a weaker field and vice-versa inducing as a result a gradual rephasing of spins. [6] Nevertheless the rephasing gradient only compensates the dephasing that is consequence of the first gradient lobe. Dephasing caused by magnetic field inhomogeneities or spin-spin interactions still cause a gradual signal intensity loss governed by[7],

$$S_{GE} = S(\alpha, T_1, S_0)\mathrm{e}^{-\frac{T_E}{T_2^*}} \tag{2.22}$$

where $T_E$ represents the echo time, $S(\alpha, T_1, S_0)$ is the signal immediately after the application of the RF-pulse which tips the magnetization vector $\alpha$ degrees towards the $xy$ plane. This equation reflects why susceptibility effects are so well enhanced by gradient echo sequences since they strongly affect $T_2^*$.
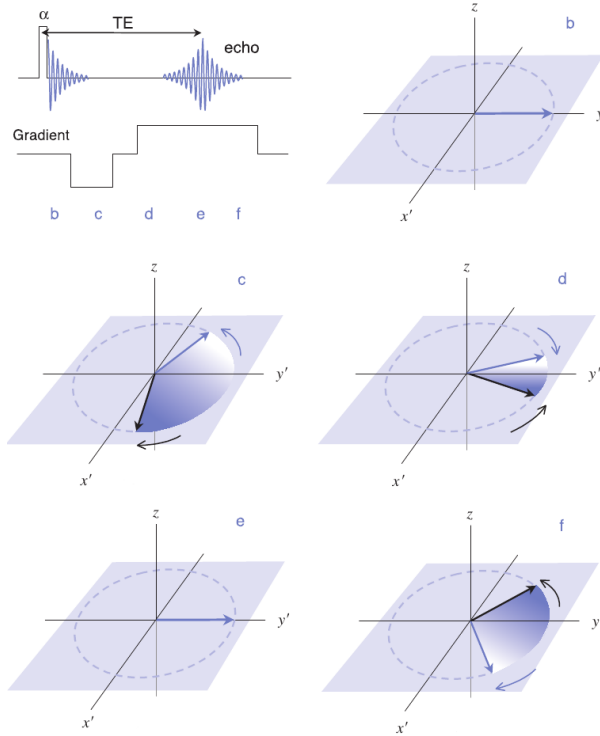
**Figure 2.4:** Example of a simple gradient-echo sequence. In $b$ spins are initially positioned along the y axis and are rapidly dephased by the negative lobe as shown in $c$. When the positive gradient is switched on ($d$), the spins begin to rephase, forming an echo ($e$). If the positive gradient is left on as show in $f$ dephasing will occur again. Adapted from [7]

This signal attenuation effect is characteristic of magnitude images, however, in SWI we are interested in the full complex description of the MR signal. With this in mind it is important to define the full signal-intensity response to a gradient echo sequence. For a right handed system as described in [5] we have:

$$S_{GE}(\alpha) = \rho_m(\alpha)e^{-i\gamma\Delta B T_E} \tag{2.23}$$

where $\alpha$ is the flip angle induced by the RF-pulse and $\Delta B$ represents the local field deviation caused by the susceptibility differences.

### 2.1.5 SPGR - Spoiled Gradient Echo

For a gradient echo sequence with $T_R >> T_2$, all transverse magnetization is zero before the next RF-pulse is applied, this is known as a spoiled gradient sequence. However this results in long acquisition times which is not practical if we want to do a certain amount of measurements with different FA. We are interested in a regime where $T_R < T_2$ (fast sequence), however

this implies that there is still some transverse magnetization prior to each RF pulse. In this situation spoiling may be obtained by applying a spoiler gradient that forces the transverse magnetization to be zero.[5]

It is important to guarantee that spoiling occurs before each RF pulse because it allows the magnetization vector to evolve towards a steady-state solution that is well known throughout the literature [5, 9, 10, 11, 12] and shown in the following equation:

$$S_{GE} \approx SPGR = \rho_0 \frac{1 - E_1}{1 - E_1 \cos(\alpha)} \sin(\alpha) \tag{2.24}$$

where, $\rho$ is the voxel proton spin density, $\alpha$ is the applied flip angle and $E_1$ is $e^{-T_R/T_1}$.

Equation 2.24 is actually known as the Ernst formula [12] and can only be applied as long as the correct spoiling before each RF pulse is guaranteed. If no spoiling is applied a transverse magnetization interference appears altering the expected signal behaviour either constructively or destructively[5, 12].

### 2.1.6   SSFP - Steady State Free Precession

The steady state free precession (SSFP) is a very fast gradient echo sequence, that makes use of both longitudinal and transverse magnetization to produce a dynamic equilibrium state for a fixed $T_R << T_2 < T1$ [10, 12, 13].

Because both longitudinal and transverse magnetization need to be taken into account on this type of MR sequence a more complex mathematical description of this signal is necessary. Assuming an initial magnetization $M_0$, relaxation variables $E_1 = e^{-T_R/T_1}$ and $E_2 = e^{-T_R/T2}$ it is possible to write out the individual components of the magnetization vector in its steady-state [5]:

$$M_x^{SS} = M_0(1 - E_1)\frac{E_2 \sin\theta \sin(\beta)}{d} \tag{2.25}$$

$$M_y^{SS} = M_0(1 - E_1)\frac{E_2 \sin\theta(\cos(\beta) - E_2)}{d} \tag{2.26}$$

$$M_z^{SS} = M_0(1 - E_1)\frac{[1 - E_2\cos(\beta)) - E_2\cos(\theta)(\cos(\beta) - E_2)]}{d} \tag{2.27}$$

where,

$$d = (1 - E_1\cos(\theta))(1 - E_2\cos(\beta)) - E_2(E_1 - \cos(\theta))(E_2 - \cos(\beta)) \tag{2.28}$$

Here, $\beta = \Delta\omega t = \gamma\Delta Bt$ is defined as the *resonance offset frequency*. This parameter is strongly dependent on the static field and since it changes
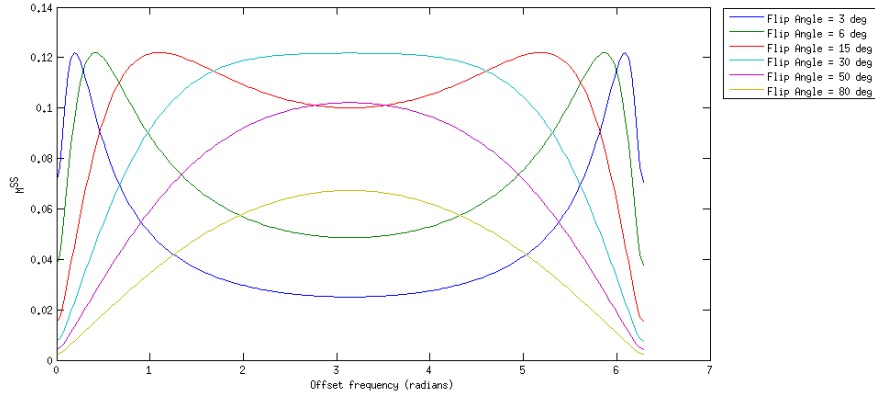
**Figure 2.5:** SSFP signal variation with offset frequency for different flip angles. $T_1 = 1086ms$, $T_2 = 69ms$ and $T_R = 3.567ms$ are fixed.

with position along the object the resulting SSFP signal is also position dependent. Figure 2.5 illustrates the SSFP signal behaviour for fixed $T_1$ and $T_2$ parameters over different flip angles as a function of offset frequency. With this in mind it is easy to anticipate that as the static field changes around an object significantly the measured signal will also change accordingly. This however, can be avoided by performing a good shimming inside the object guaranteeing as low field variation as possible.[5]

## 2.2 SWI - Susceptibility Weighted Imaging

One of the goals of this thesis is to adapt SWI, initially developed for the adult brain, to the neonatal brain. In order to accomplish this objective a good understanding of how this kind of images are obtained is required, and therefore a introductory discussion of the concepts needed to understand this type of MR imaging is presented within this section.

### 2.2.1 Comprehending SWI

Interpreting SW images for clinical diagnostic purposes, requires special care so that correct information is obtained. There are 3 major components that must be taken into account[1], the first component is the magnitude data. Gradient echo magnitude images clearly reflect areas with either short $T_2^*$ or an oscillatory signal intensity caused by the presence of deoxyhaemoglobin(dHb) in the major veins, with the latter being the main responsible factor for the signal loss visible in these images. For a subvoxel sized vein, this signal loss results in hypointense voxel relative to its

surroundings, while on the other hand, a voxel containing only intravenous signal will not show this cancellation effect, and therefore the vein appears bright inside with a hypointense ring around it.[1]

The second relevant component is the phase image. Depending on the scanner manufacturer's adopted convention,[14] veins will have negative phase values (because of the paramagnetic property of dHb) while calcium deposits will have positive phase values (because calcium is diamagnetic)[1], or vice-versa.

The third component is the processing required to obtain the final SW image. By combining $T_2^*$ decay suppression effects presented on the magnitude information and venous blood susceptibility differences relative to its surroundings recorded in the phase image, one single set of SW images is produced that enhances small veins present in the human brain. The venous vessels usually appear as black dots across each imaged slice representing cross-sections of them. The mIP is therefore performed in order to check the connectivity of these dots along different slices, and allowing clinicians to distinguish between blood vessels and micro-bleeds.[1]

Within the following sections a more complete description of what magnetic susceptibility is as well as of each component will be presented, so that a correct understanding of the work presented in Chapter 3 is accomplished.

### 2.2.2 Magnetic Susceptibility

Susceptibility information complements that available with conventional spin density, $T_1$-, and $T_2$-weighted imaging.[1] In order to understand how SWI may provide different clinical information it's important to understand what susceptibility is and how it can help us map different tissues when in the presence of deoxygenated blood, iron or calcium.

Magnetic susceptibility is related to the conformational response of a substance when placed inside an external magnetic field. When inside an uniform magnetic field the bulk magnetization $\vec{M}_B$ induced on a substance is given by,

$$\vec{M}_B = \chi \vec{H} \tag{2.29}$$

recalling that the magnetic field induced ($\vec{B}$) on a substance exposed to a magnetic field strength $\vec{H}$ is $\vec{B} = \mu_0(\vec{H} + \vec{M}_B)$ we obtain,

$$\vec{B} = \mu_0(\vec{H} + \vec{M}_B) = \mu_0(1 + \chi)\vec{H} = \mu_0\mu_r\vec{H} = \mu\vec{H} \tag{2.30}$$

where $\mu$, $\mu_o$ and $\mu_r$ are respectively the magnetic permeability of the substance, the magnetic permeability in vacuum and the relative magnetic per-

meability. From Equation 2.30 we may obtain,

$$\vec{M}_B = \chi\vec{B}/\mu_0(1+\chi) \tag{2.31}$$

which for linear materials where $\chi \ll 1$, leads to

$$\vec{M}_B = \chi\vec{B}/\mu_0 \tag{2.32}$$

from which we may conclude that the induced magnetization is directly proportional to the main magnetic field and the magnetic susceptibility[1] suggesting that depending on the tissue composition we may obtain different local fields, therefore opening a window for susceptibility mapping since the Larmor frequency is directly dependent on the local field.

### 2.2.2.1 Geometry Effects

Magnetic susceptibility distorts the uniform field outside an object as a function of its geometry. Following the description presented in [1] and [15], the local field variation inside a cylinder placed at an angle $\theta$ relative to the main field $B_0$ is given by[1], [5],

$$\Delta B_{in} = \Delta\chi B_0(3\cos^2\theta - 1)/6 + \chi_e B_0/3 \tag{2.33}$$

where $\Delta\chi = \chi_i - \chi_e$ and $\chi_e$ and $\chi_i$ are the susceptibilities outside and inside the cylinder. Usually when looking at local field changes, the term $\chi_e B_0/3$ is constant both inside and outside the cylinder and therefore may be dropped when considering field variations between different tissues. $\Delta\chi$ may be estimated for the case of deoxygenated blood as,

$$\Delta\chi = 4\pi A(0.18\text{ppm})\text{Hct}(1-Y) \tag{2.34}$$

where $A$ is a constant determined by the susceptibility of blood in vivo, Hct is the hematocrit, and $Y$ is the oxygen saturation.[1, 16, 17]

For the field variation outside the considered vessel, by taking $a$ as the vessel radius, which is considered as a long cylinder positioned at an angle $\theta$ relative to the main field, $r$ is the distance perpendicularly from the axis of the cylinder to the considered position and $\Phi$ is the angle between the vector $r$ and the projection of the main field direction onto a plane perpendicular to the axis of the vessel[1, 5], we obtain the following relationship resulting in the field distribution shown in Figure 2.6:

$$\Delta B_{out} = \Delta\chi B_0 \sin^2\theta\cos(2\Phi)a^2/(2r^2) \tag{2.35}$$

The key point of presenting this field variation with geometry is to relate this information to the signal phase of equation 2.23 and verify that:

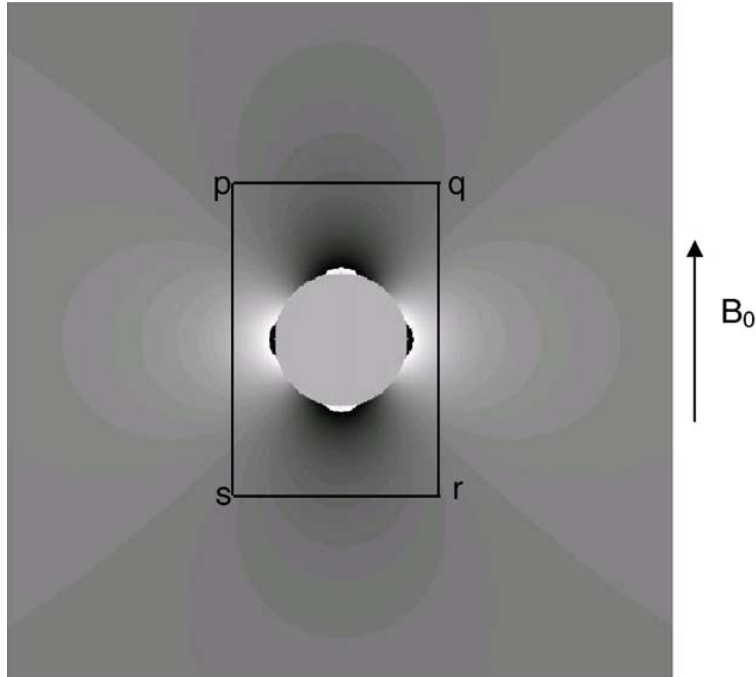$$\Delta\phi = -\gamma\Delta B T_E \tag{2.36}$$

**Figure 2.6:** Magnetic field distribution resulting from a cylinder placed perpendicular to $B_0$. Adapted from [18].

and therefore, the phase variation is dependent on the vessel geometry.[1, 18, 19, 20]

When susceptibility-induced local field variations are present within an imaging voxel, there is a resulting distribution of Larmor frequencies for the protons within that voxel, resulting in signal loss which is the source of Blood oxygen level-dependent (BOLD) contrast.[21] In 1997, Reichenbach et al.[22], showed that with the right pulse sequence, it is possible to depict blood vessels with diameters of less than a millimeter by making use of the BOLD effect. The next section shows how this signal variation in the phase image can be used to identify signal variations produced by dHb in order to enhance visualization of small veins in the human brain.

### 2.2.2.2 Phase Filtering for Highlighting Susceptibility Variations

Background field inhomogeneities tend to cause low spatial frequency phase variations[19]. Also, because one is only capable of mapping phase variations within the $[-\pi, \pi)$ interval phase wrappings occur, making it harder to identify useful phase information. Fortunately we are only interested in highlighting local susceptibility variations which correspond to high fre-

quency information in the phase image. With this in mind, as described in [19] it is possible to remove phase wrapping and inhomogeneity effects by complex dividing the original image with the image obtained by low-pass-filtering (LP-filter) k-space data, and therefore, obtaining a high-pass-filter (HP-filter) effect on the image.

Taking a more mathematical approach, if we consider the original complex signal $\rho_0(x)$,

$$\rho_0(x) = |\rho_0(x)| e^{i\phi_f(x) + i\phi_v(x)} = F^{-1}[S(k)] \tag{2.37}$$

as being the complex image information, where $F$ is the Fourier transform operator, $\phi_f(x)$ is the phase component which we assume to correspond to background variations, $\phi_v(x)$ contains local susceptibility variations of interest such as venous blood information, and $S(k)$ is the original k-space information. For simplicity only these two components are considered but other sources of magnetic field variations also contribute to both $\phi_f(x)$ and $\phi_v(x)$

As stated above we assume that background field inhomogeneities only generate low frequency variations and therefore, by truncating the original data and zero padding the resulting k-space to have the same size as the original k-space information, we obtain a low-pass filter effect (n point $H(k)$ filter). The obtained low-pass filtered image is then:

$$\rho_{lp}(x) = |\rho_{lp}(x)| e^{i\phi_f(x)} = F^{-1}[S(k)H(k)] \tag{2.38}$$

We may then use this information to complex divide the original image so that,

$$\rho_{hp}(x) = \frac{|\rho_0(x)| e^{i\phi_f(x) + i\phi_v(x)}}{|\rho_{lp}(x)| e^{i\phi_f(x)}} \approx |\rho_{hp}(x)| e^{i\phi_v(x)} \tag{2.39}$$

The phase $\phi_v(x)$ is now approximately free of low-frequency variations. An example of this process is demonstrated in Figure 2.7. As seen in Figure 2.7 (b) vessel information is highlighted suggesting that this approach may allow vessel topography with deoxygenated blood as a natural occurring contrast agent.

### 2.2.3 Creation of SWI

SWI aims to create a different type of MRI contrast that complements the information from conventional $T_1$ and $T_2$ sequences. This is done by making use of both magnitude and phase information of a transversal 3D spoiled gradient echo MR signal with low white matter to gray matter contrast, allowing susceptibility effects to be mapped in the magnitude image after
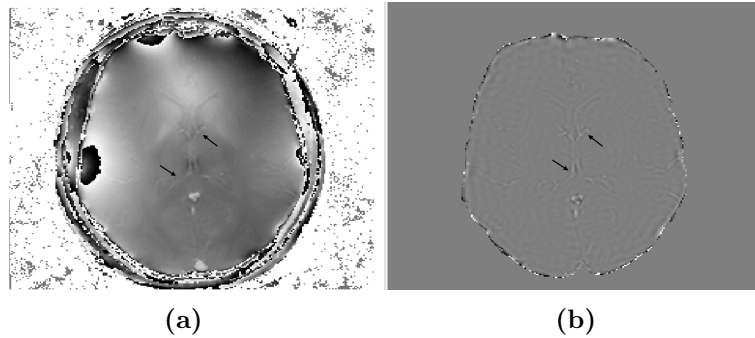
**(a)**            **(b)**

**Figure 2.7:** (a) Raw phase image of an adult human brain. It is possible to see phase wraps specially close to the border of the brain. (b) Same image presented in (a) after applying the High Pass filter discussed in section 2.2.2.2. It is possible to see that vessel information is highlighted (black arrows).

some post-processing.

In 2000, Y. Wang et al.[19], suggested using HP-filtered phase images in order to produce phase masks that could be applied to the commonly used magnitude image in order to enhance susceptibility effects and therefore depict small blood vessels. This so called phase-masks[1, 19, 14, 23] are the key-point of SWI's ability to produce venographic images. Once they are applied to the magnitude image they enhance small vessel contrast relative to the background and therefore increase the ability to depict them.

### 2.2.3.1 Phase Mask
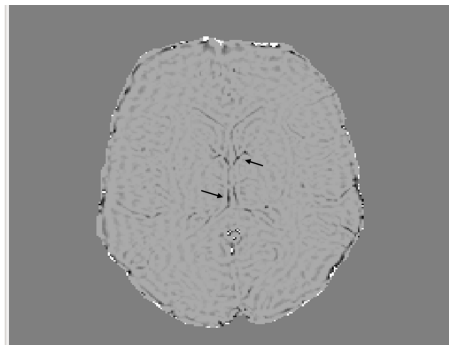


**Figure 2.8:** Brain mask extracted from HP-filtered image show in Figure 2.7 b). All positive phase values were linearly scaled to the $[0, 1]$ interval as described in this section. The black arrows indicate areas where vessels are present and therefore they were linearly scaled to values close to 0 in the phase mask.

There are several different phase masks that may be extracted from the phase image depending on what phase information is considered relevant to

enhance venographic contrast. According to [19], and because of the local field behaviour discussed in section 2.2.2.1, the venous blood phase should be either negative or positive depending on the vein orientation relative to the main magnetic field.

More precisely three orientation intervals should be considered, corresponding to angles smaller than $55°$ (positive phase), values close to $55°$ (null phase) and values larger than $55°$ (negative phase).[19] However, this predicted behaviour is not respected thanks to partial volume effects that must be taken into account.[18] Y. Xu et al.[18], studied how different voxel sizes and positions relative to a long cylinder positioned perpendicularly to the main magnetic field change the measured phase, introducing the concept of voxel aspect ratio. Also, it is important to note, that the convention used to define positive phase is not the same for all vendors and therefore special care must be taken in order to accommodate this issue[14].
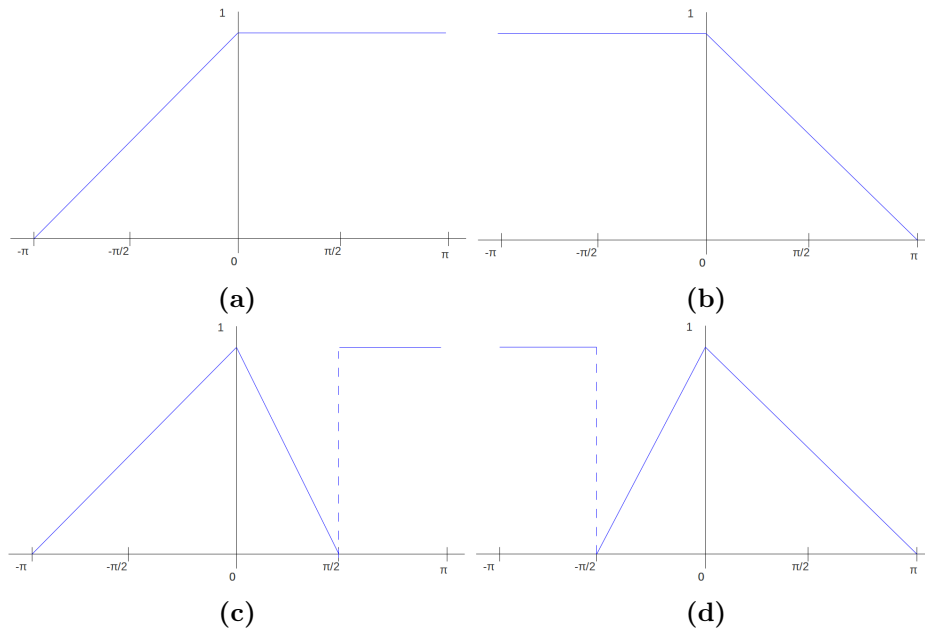


**Figure 2.9:** Comparison between different phase masks proposed by different authors in literature. a) negative phase mask, b) positive phase mask, c) asymmetric negative phase mask, d) asymmetric positive phase mask

Once the correct phase of interest is chosen the phase mask (Figure 2.8) is generated by performing a linear scaling that sets to 1 the pixels with phase values that we want to keep unchanged and sets to 0 pixels with phase values that we want to suppress (Figure 2.9). By selecting an appropriate voxel aspect ratio it is possible to obtain phase values that lie in the

$[-\pi, 0)$ or in the $(0, \pi]$ interval[18]. Therefore, as an example, if the phase of interest lies within the $(0, \pi]$ interval, the phase mask is defined by setting all values on the $[-\pi, 0)$ interval to unity, and setting the $(0, \pi]$ interval as $\phi_{scaled} = -\phi_{measured}/\pi + 1$. An example of this so called positive filter, or positive phase mask applied to an adult human brain is shown in Figure 2.8. This approach leads to a maximum signal cancellation for veins in parallel orientation relative to the main magnetic field, and also gives good results for vessels perpendicular to $B_0$[20]. More examples of proposed phase masks found in the literature are presented in Figure 2.9.

### 2.2.3.2 Minimum Intensity Projection - mIP

After selecting the appropriate phase mask, the SWI processing assembly line ends with a minimum intensity projection (mIP) of a selected range of contiguous slices of the image that results from the multiplication of the original magnitude image by the extracted phase mask[20]. Since the phase mask was designed to suppress high susceptibility pixels while maintaining the rest intact, this multiplication enhances venographic contrast, by imposing a susceptibility weighting on the magnitude image. A mIP is then performed in order to project a topographic effect that helps keep track of the vessels through different imaged slices therefore giving a 3D angiography effect. An example of the mIP projection can be seen in Figure 2.10.
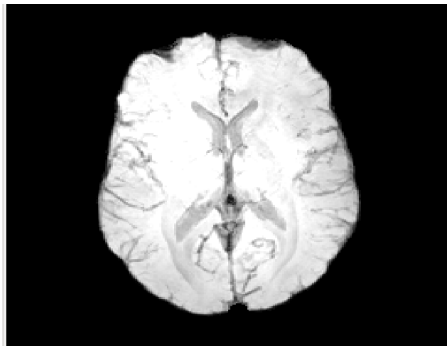


**Figure 2.10:** Minimum Intensity Projection of the multiplication of Figure 2.8 by its respective magnitude image. It is possible to track some venous paths suggesting SWI is a good tool for venographic mapping.

### 2.2.3.3 Voxel Aspect Ratio

One important aspect of SWI that was not yet discussed within this thesis is the role of the acquisition voxel size and position relative the imaged vessels. Because of the variety of vessel sizes presented inside the human brain, studies which aim to optimize acquisition voxel size in order to obtain good

global vessel visualization, have been previously presented [18, 24]. Defining voxel aspect ratio (AR) as being the ratio between voxel thickness and voxel in-plane resolution, the work published by Yingbiao Xu in 2005 [18], suggests that a theoretical AR of 2 should be used for best vessel visualization, however they found that in practice an AR of 4 gives better visualization. Therefore it is common practice to acquire SWI with an AR of either 2 or 4.

### 2.2.4   SWI - Neonate Approach

The neonatal brain has a higher water content $(92 - 95\%)$ than the adult brain $(82-85\%)$, and as a consequence of that $T_1$ and $T_2$ values are larger.[25] This means that when scanning neonates optimal $T_E$ and $T_R$ must be chosen to compensate for this higher water content. For an adult SW brain scan at 3T field strength, the typical MR parameters are $T_R = 30$ms and $T_E = 20$ms as presented in [1], on the other hand, typical neonatal SW imaging acquisition parameters as presented by [26] are $T_R = 52$ms and $T_E = 30$ms.

## 2.3   DESPOT - Driven Equilibrium Single Pulse Observation of T1 and T2

Driven equilibrium Single Pulse Observation of $T_1$ and $T_2$ (DESPOT) originally called variable nutation angle method was first introduced as a way to estimate $T_1$ by applying a set of spoiled gradient echo sequences (SPGR) over different flip angles [9]. The DESPOT nomenclature was first introduced by John Homer and Martin S. Beevers in 1985 [9] and further expanded to DESPOT1 and DESPOT2 by Deoni et al. in 2003 [10] when they suggested the use of a steady-state free precession sequence (SSFP) to map $T_2$ information after $T_1$ had been assessed.

In simple terms DESPOT1 and DESPOT2 (referred to as DESPOT in this text) consists in acquiring a set of measurements over different flip angles (FA) and fitting the expected behaviour in order to estimate $T_1$ and $T_2$ relaxation times inside each voxel. To fully understand how this is possible it is important to comprehend the physical processes behind each signal in order to be able to predict the obtained results.

### 2.3.1   Obtaining $T_1$ and $T_2$ from collected data

The parameters of interest $T_1$ and $T_2$ are obtained from a set of SPGR and SSFP images acquired at fixed $T_R$ and incrementally increased flip angle $\alpha$.

Following the description presented in [10] the SPGR can be represented in the linear form by:

$$\frac{S_{SPGR}}{\sin(\alpha)} = E_1 \frac{S_{SPGR}}{\tan(\alpha)} + M_0(1 - E_1) \tag{2.40}$$

from which the slope $m$ and Y-intercept $b$ can be estimated by linear regression, allowing us to extract $T_1$ and $M_0$ as being:

$$T_1 = -T_R/ln(m) \tag{2.41}$$

$$M_0 = b/(1 - m) \tag{2.42}$$

Afterwards, $T_1$ is used in order to fit $T_2$ from the linearised version of the SSFP equations:

$$\frac{S_{SSFP}}{\sin(\alpha)} = \frac{E_1 - E_2}{1 - E_1 E_2} \times \frac{S_{SSFP}}{\tan(\alpha)} + \frac{M_0(1 - E_1)}{1 - E_1 E_2} \tag{2.43}$$

where, also by linear regression we obtain a new $m$ and $b$ resulting in,

$$T_2 = -T_R/ln(\frac{m - E_1}{mE_1 - 1}) \tag{2.44}$$

$$M_0 = b(E_1 E_2 - 1)/(1 - E_1) \tag{2.45}$$

Within this thesis, it was decided that instead of linearising the problem and fitting first for $T_1$ and then for $T_2$ a more interesting approach would be to simultaneously fit for $T_1$ and $T_2$ using MatLab 2012a optimization routine *fminsearch*. A more complete description of this optimization procedure is described in Chapter 4.

### 2.3.2 mcDESPOT - Multi Component DESPOT

A limitation of the DESPOT method for estimating $T_1$ and $T_2$ is the assumption of a single source of signal inside each voxel[27]. This assumption ignores the inherently complex structure of biological tissues. In order to overcome this issue, Deoni et al. presented in 2008 a very interesting paper [27] in which a two exchanging water-pools model was proposed in order to explain the observed signal inside each voxel. Following previous work presented by Spenser and Fishbein [11] and Deoni et al.[28, 29], a fast decaying pool corresponding to trapped water inside myelin ($F$) and a slower decaying pool corresponding to water outside the myelin sheet ($S$) where considered. With this in mind the total equilibrium magnetization $M_0$ results from the sum of individual fractional proton densities ($f_F$ and $f_S$) with their corresponding decay rates $T_{1,F} = 1/R_{1,F}$, $T_{1,S} = 1/R_{1,S}$, $T_{2,F} = 1/R_{2,F}$ and

$T_{2,S} = 1/R_{2,S}$. Assuming a constant exchange rate $(k)$ between the two pools $(k_{FS} = 1/\tau_{FS}$ and $k_{SF} = 1/\tau_{SF})$ at equilibrium we have

$$f_F k_{FS} = f_S k_{SF} \tag{2.46}$$

and,

$$f_S = 1 - f_F \tag{2.47}$$

resulting in a seven dimensional problem that needs to be solved for $M_0$, $k_{FS}$, $f_F$, $T_{1,F}$, $T_{2,F}$, $T_{1,S}$ and $T_{2,S}$. By incorporating this set-up into the Bloch-McConnell equations (Equation 2.48) we obtain:

$$\frac{d\mathbf{M}}{dt} = \mathbf{AM} + \mathbf{C} \tag{2.48}$$

Assuming a periodic instantaneous excitation along the x-axis, the steady state solution to this problem may be found as [11, 27, 29, 30, 31]

$$M_{SSFP}^{SS} = [\mathbf{I} - e^{\mathbf{A}_{SSFP}T_R}\mathbf{R}(\alpha)]^{-1}(e^{\mathbf{A}_{SSFP}T_R} - \mathbf{I})\mathbf{A}_{SSFP}^{-1}\mathbf{C} \tag{2.49}$$

where,

$$M_{SSFP}^{SS} = \begin{bmatrix} M_{x,F}^{SS} & M_{x,S}^{SS} & M_{y,F}^{SS} & M_{y,S}^{SS} & M_{z,F}^{SS} & M_{z,S}^{SS} \end{bmatrix}^T \tag{2.50}$$

$A_{SSFP} =$

$$\begin{bmatrix} -R_{2,F} - k_{FS} & k_{SF} & \Delta\omega & 0 & 0 & 0 \\ k_{FS} & -R_{2,S} - k_{SF} & 0 & \Delta\omega & 0 & 0 \\ -\Delta\omega & 0 & -R_{2,F} - k_{FS} & k_{SF} & 0 & 0 \\ 0 & -\Delta\omega & k_{FS} & -R_{2,S} - k_{SF} & 0 & 0 \\ 0 & 0 & 0 & 0 & -R_{1,F} - k_{FS} & k_{SF} \\ 0 & 0 & 0 & 0 & k_{FS} & -R_{1,S} - k_{SF} \end{bmatrix}$$
$$\tag{2.51}$$

$$R_\alpha = \begin{bmatrix} 1 & 0 & 0 & 0 & 0 & 0 \\ 0 & 1 & 0 & 0 & 0 & 0 \\ 0 & 0 & \cos(\alpha) & 0 & \sin(\alpha) & 0 \\ 0 & 0 & 0 & \cos(\alpha) & 0 & \sin(\alpha) \\ 0 & 0 & -\sin(\alpha) & 0 & \cos(\alpha) & 0 \\ 0 & 0 & 0 & -\sin(\alpha) & 0 & \cos(\alpha) \end{bmatrix} \tag{2.52}$$

$$C = \rho \begin{bmatrix} 0 & 0 & 0 & 0 & f_F R_{1,F} & f_S R_{1,S} \end{bmatrix} \tag{2.53}$$

The measured signal is therefore $M_{x,F}^{SS} + M_{x,S}^{SS} + i(M_{y,F}^{SS} + M_{y,S}^{SS})$. The SPGR signal can be viewed as a more specific solution to the Bloch-McConnell equation where all transverse magnetization is set to zero prior to each rf-pulse. In this case the solution to Equation 2.48 becomes[27, 31]

$$M_{SPGR}^{SS} = M_0 \sin \alpha [I - e^{A_{SPGR}T_R} \cos \alpha]^{-1} (I - e^{A_{SPGR}T_R}) \begin{bmatrix} f_F \\ f_S \end{bmatrix} \qquad (2.54)$$

with,

$$A_{SPGR} = \begin{bmatrix} -R_{1,F} - k_{FS} & k_{SF} \\ k_{FS} & -R_{1,S} - k_{SF} \end{bmatrix} \qquad (2.55)$$

This set of equations constitute the two-pool model of DESPOT. One flaw that can be assigned to this two-pool model is that it doesn't take into account partial volume effects i.e., voxels containing brain tissue and ventricle or meninges, result in myelin water fraction underestimation [30]. In order to overcome this issue, Deoni et al. presented in 2012 a three-pool model that incorporated a new, non-exchanging "free water" component. The three-pool model is similar to the two-pool model and a complete description may be found in [30].

# Chapter 3

# Susceptibility Weighted Imaging of the Neonatal Brain

As stated in section 2.2, SWI is very sensitive to susceptibility variations between oxygenated and deoxygenated haemoglobin.[32] In the same section the common SWI processing pipeline was also described. In this chapter the gold standard SWI protocol for the adult brain is presented alongside with its adaptation to the neonatal brain which is known to have longer relaxation times.[25]

## 3.1  SWI Adult Protocol

A review of the literature confirmed that the protocol provided by Haacke et al. in their 2009 review paper [1] is in fact standard. Here, they stated that in order to obtain optimum vein contrast at 1.5T, an echo time (TE) between 40 and 80 ms must be chosen. Furthermore, if we recall from section 2.2.2.1 the linear relationship between phase and field strength it is straightforward to understand that with a field strength of 3T the optimal TE values would drop to between 20 and 40 ms.

According to [15, 33, 34], the typical SWI adult protocol on a 3T MR system involves a 3D, fully flow-compensated gradient echo sequence using the following parameters:

- $T_E \approx 20$ ms

- $T_R \approx 30$ ms

- Flip Angle $\approx 15°$

- voxel size between 0.5 mm ×0.5 mm ×1.5 mm and 1 mm ×1 mm ×4 mm

- Employing either SENSE (sensitivity encoding) or GRAPPA (generalized autocalibrating partially parallel acquisitions) for acceleration typically with a factor of 2

- Total acquisition time between 3 to 7 min

The data is then exported from the scanner, and post-processed offline using in-house developed pipelines.
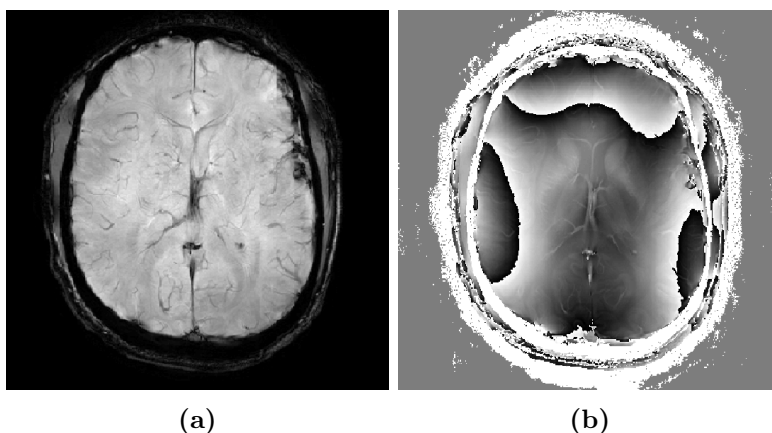


(a)                                    (b)

**Figure 3.1:** (a) Magnitude image of an adult human brain obtained with the proposed protocol. It is possible to see blood vessels as hypo-intense signals. (b) Phase image of the same brain presented in (a). It is possible to see that vessel information is highlighted.

As a first step towards implementing SWI in the neonatal brain, a neonatal protocol was proposed based on simulations over a range of $T_1$ and $T_2$ tissue parameters expected in the neonatal brain as described further in this thesis (section 3.4):

- $T_E = 25$ ms

- $T_R = 32$ ms

- Flip Angle $= 12°$

- voxel size 0.5 mm ×0.5 mm ×2 mm

- SENSE factor 2

This protocol was used as starting point for developing the SWI post-processing pipeline and protocol adaptation towards the neonatal brain.

In order to have some test data to develop the necessary post-processing
scripts the proposed neonatal protocol was tested on an adult volunteer
(Figure 3.1). The data was acquired on a Philips 3T Achieva scanner and
informed consent was given by the volunteer according to a local ethical
approval. A magnitude and phase image obtained with this protocol is
presented in Figure 3.1.

## 3.2  Exploring Phase Information

As stated in [14], phase information depends on manufacturer convention.
This means that the same venous vessel may appear with positive phase on a
Phillips scanner and negative on a Siemens scanner depending on the phase
convention that each system uses. Therefore it is of highest importance to
fully understand which phase information we are interested in so that we
can correctly apply the filters described in section 2.2.2.2. Looking more
carefully to the phase image obtained (Figure 3.2) we can see that the vessel
information is positive and therefore the phase mask in the post-processing
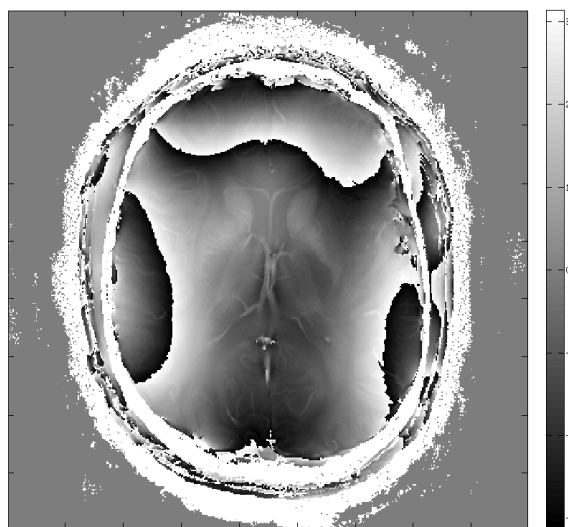pipeline (section 2.2.2.2) should also be positive.



**Figure 3.2:** Transversal slice of an adult brain phase image. In the image scale
all values range from $-\pi$ to $\pi$. It is important to see that vessel information has
positive phase.

## 3.3 Development of a Graphical User Interface

The post-processing scripts that allow the creation of SWI from both the magnitude and phase images, were developed by integrating MatLab 2012a with FSL-FMRIB Software Library v5.0. However for users which are not familiar with programming environment the use of scripts to obtain clinical relevant data may become confusing. With this in mind, in order to facilitate this processing step a graphical user interface (GUI) was developed in MatLab 2012a with the *guide toolbox* environment(Figure 3.3).
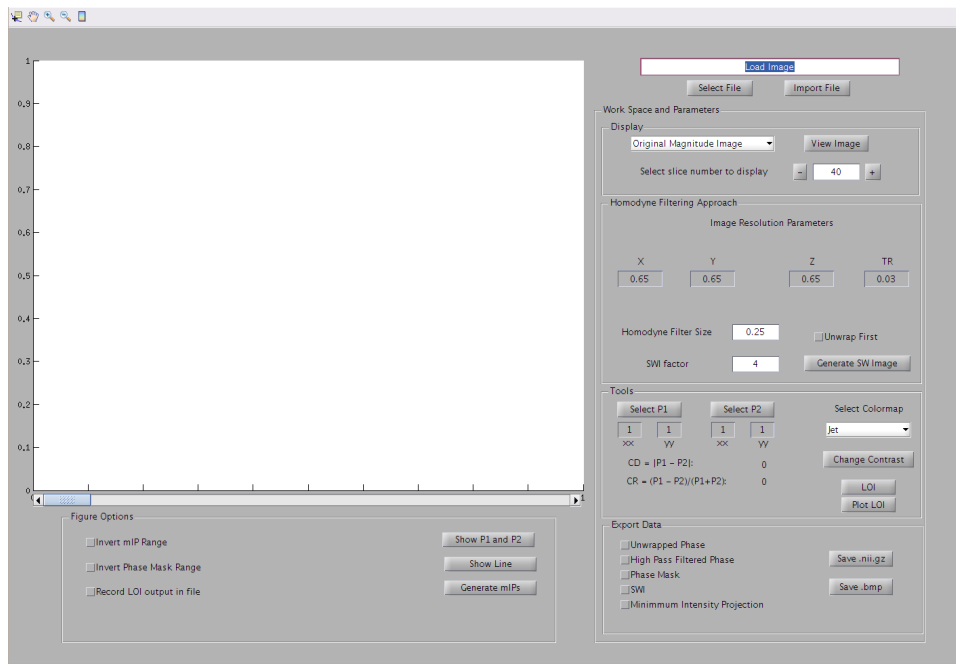


**Figure 3.3:** Graphical User Interface (GUI) developed in order to facilitate the application of the SWI processing pipeline.

This interface assumes a .PAR/.REC image file, as exported from Philips Scanners. The "Select File" and "Import File" buttons, allow the user to browse until finding the desired file and import it. The Display section (Figure 3.4) has a drop-box that allows the user to switch between different types of images that will be displayed in the blank space in Figure 3.3. Initially, it only allows the user to chose between magnitude and phase images, after the SWI is created then it also allows the user to view the susceptibility weighted image, the high-pass filtered image and the positive and negative phase mask images.

The Homodyne Filtering Approach Section (Figure 3.5) allows the user to easily define the homodyne filtering parameters, where the filter size must
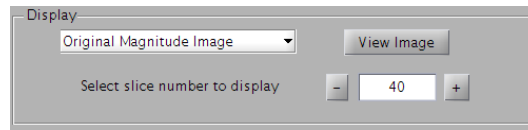
26

**Figure 3.4:** SWI GUI Display Section. Allows the user to select which images
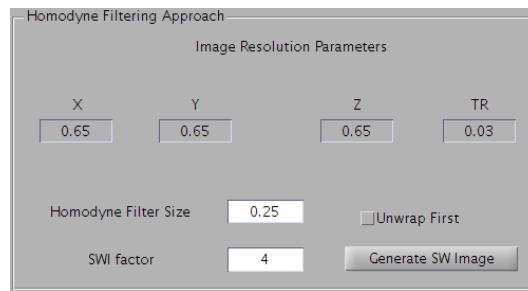should be displayed by the interface.

**Figure 3.5:** SWI GUI Filtering Section. This section allows the user to easily
define the homodyne filtering parameters, the filter size must be defined as a
fraction of the phase encoding steps, SWI-factor is defined as the number of times
the phase-mask is applied to the magnitude image, the Image Resolution
parameters needs to be defined by the user.

be defined as a fraction of the phase encoding steps. SWI-factor is defined
as the number of times the phase-mask is applied to the magnitude image,
while the Image Resolution parameters must be defined by the user. The
"Generate SW Image" button uses the defined parameters to generate the
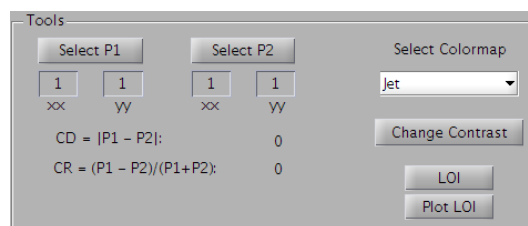susceptibility weighted image.

**Figure 3.6:** SWI GUI Tools Section. This section offers the possibility to define
two points and compute the contrast by difference (CD) and the contrast ratio
(CR) between them. The "LOI" and "Plot LOI" buttons allow the user to draw,
compute and plot the CR along the line length.

The Tools section in Figure 3.6 allows the user to analyse the displayed
slice. Two points can be be selected by pressing the "Select P1" and "Select
P2" buttons, or by typing the image pixel coordinate in the respective space,
in order to compute the contrast by difference ($CD = |P_1 - P_2|$) and the
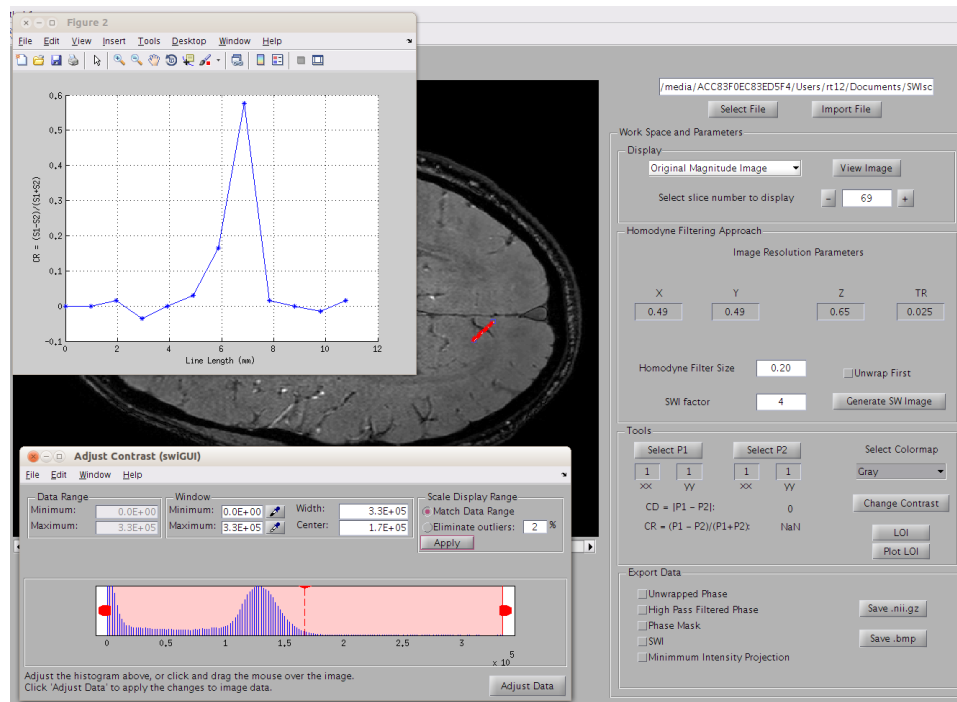
**Figure 3.7:** Example of the plot obtained from the "LOI" and "Plot LOI"
buttons. The plot in blue (left-top corner) is the CR over the length of the red
line drawn in the image.

contrast ratio $(CR = (P_1 - P_2)/(P_1 + P_2))$. The "Change Contrast" button
opens a small MatLab tool named *imcontrst* that allows the user to change
the displayed image contrast to better view some structures. The "LOI"
and "Plot LOI" buttons allow the user to draw a line, compute and plot the
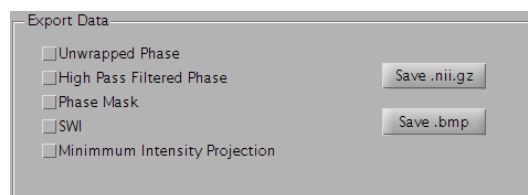CR along the line length (Figure 3.7).



**Figure 3.8:** SWI GUI export section, this allows the user to export the ticked
images.

The export section in Figure 3.8 allows the user to export the ticked
images either in "NIFTI" format or in ".bmp" format.

To finalize there is the Figure Options section (Figure 3.9). This sec-

28

tion has three buttons that allow the user to show the previous selected
points and line ("Show P1 and P2" and "Show Line" buttons) and a "Generate mIPs" button that generates a minimum intensity projection image
of the previously computed SWI. The tick-boxes "Invert mIP Range" and
"Invert Phase Mask Range" allow the user to invert the image scale of the
minimum intensity projection and the phase masks in order to give a more
angiography-like effect. The tick-box "Record LOI output in file" when
ticked records the data analysed along each drawn line to an output file in
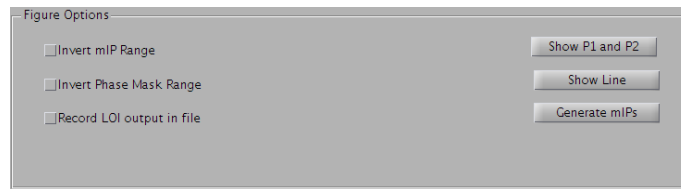order to be analysed later.



**Figure 3.9:** SWI GUI Figure Options sections.

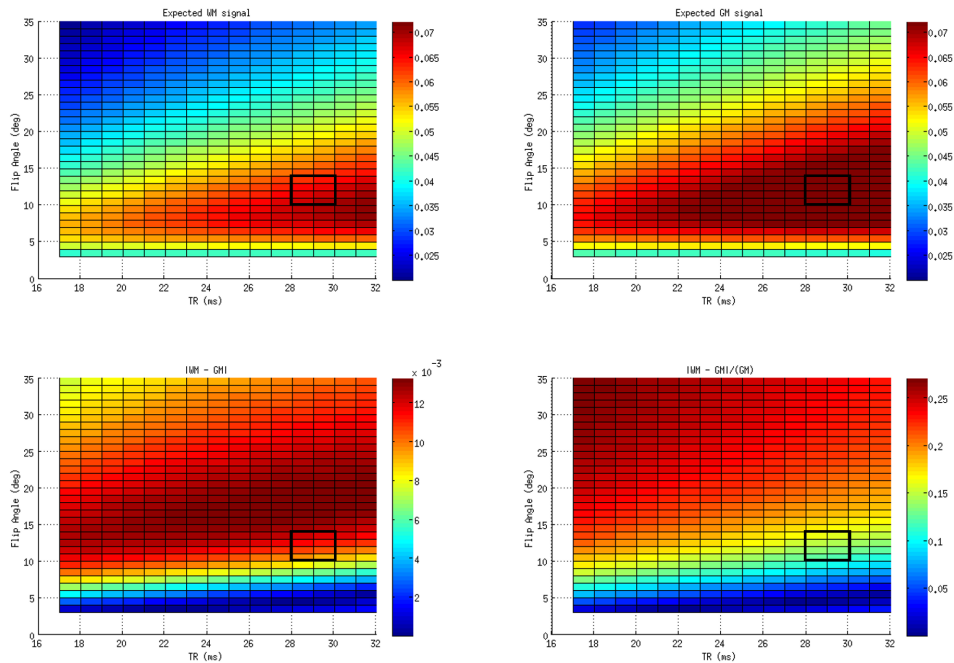## 3.4   Neonatal Protocol



**Figure 3.10:** This figure represents how the signal and relative contrast changes
over different echo times and flip angles.

As stated previously in this text(section 2.2.4) the relaxation times in the
neonatal brain are different from the adult brain.[25] Therefore it is neces-
sary to optimize the sequence parameters (TE and FA) in order to obtained
a low WM/GM contrast with as high signal intensity as possible, the low
WM/GM contrast is important because in SWI we are not interested in this
type of contrast but on using the magnitude image to map susceptibility ef-
fects. In order to assess this a plot of the CR over different $T_R = T_E + 7$ (the
number 7ms is the minimum time difference allowed by the scanner between
$T_R$ and $T_E$) ms and FA parameters was done (Figure 3.10). This simulation
assumed white matter relaxation times of $T_1 = 2500$ ms and $T_2 = 240$ ms
and gray matter relaxation times of $T_2 = 1800$ ms and $T_2 = 144$ ms [35].

By analysing Figure 3.10 one can decide on a good compromise between
expected signal intensity and desired contrast. As stated above in this text,
in SWI we are interested in obtaining images with as low WM/GM contrast
as possible while guaranteeing a good signal intensity, it was therefore de-
cided, by inspecting Figure 3.10 to test a range of repetition times between
28 ms and 32 ms and a range of flip angles between $10°$ and $14°$. This range
of parameters was tested on a Philips 3T Achieva scanner and data was
obtained on newborns less than one week old with informed consent given
by their parents according to local ethical approval requirements, in order
to assess which set of parameters would give a good result.

## 3.5   Revisiting Voxel Aspect Ratio

In section 2.2.3.3 a small introduction on the gold-standard SWI voxel ac-
quisition size was presented. This kind of voxel ratio allows an excellent
visualisation of the transversal plain, however, information from the other
two planes of view (Sagittal and Coronal) is much worse.
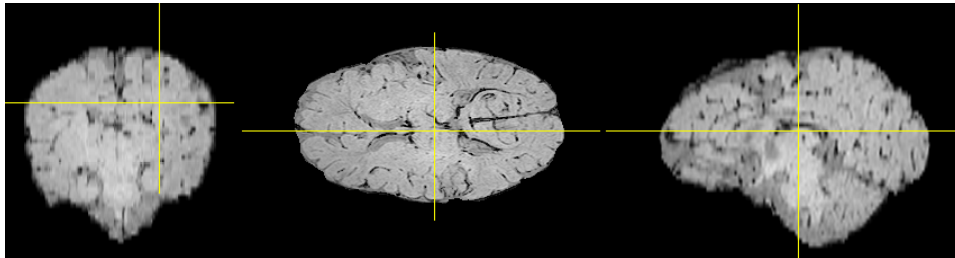


**Figure 3.11:** Susceptibility Weighted Image of a baby brain acquired with
in-plain resolution of 0.65 mm ×0.65 mm and a voxel thickness of 2.6 mm.

Looking at Figure 3.11 we can see that the obtained SNR is very good

and the vessel structures are very well depicted. But we are interested in
being able to visualize these structures over all three planes, so, in order
to accomplish this goal we suggest to, instead of acquiring images with a
1:4 voxel ratio, to do it with a 1:1 voxel ratio. Deistung et al. showed in
their 2008 paper [24] how SWI contrast changes with different voxel AR.
According to this study, best SWI contrast is obtained for AR larger than 2,
however within this thesis it was decided that the predicted loss in contrast
from an AR of 1 compared to an AR $> 2$ does not compensate the loss of
relevant information in the Sagittal and Transversal planes of view. An AR
of 1 will reduce the SNR per voxel but, on the other hand, it will allow us
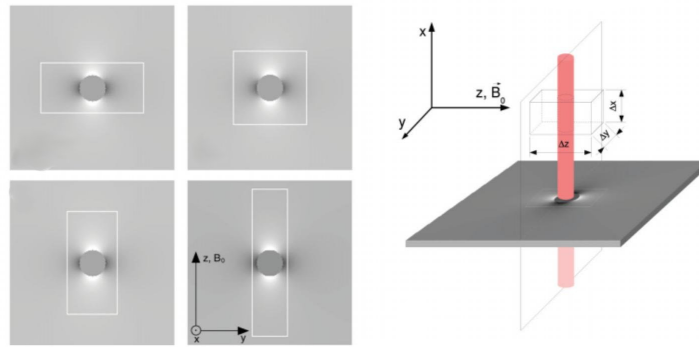to visualise vessel information on all three directions.



**Figure 3.12:** Magnetic field distribution resulting from a cylinder perpendicular
to a static magnetic field $B_0$. The white boxes indicate voxels with aspect ratios
of 0.5, 1, 2, and 4. The geometric relationship voxels, vein and field distribution
are shown in the right side figure. Adapted from [24]

Special care must be taken when changing the AR to 1 because of the
expected phase distribution shown in Figure 3.12. When using an AR of 4
the positive mask was more favourable in order to guarantee that only the
signal at the center of the vessels is decreased. However for a 1:1 ratio we
found it to be more favourable to adopt a positive phase mask to enhance
vessels in transverse plane, while using a negative phase mask to enhance
vessels in the Sagittal and Coronal planes (Figure 3.13). In this way the
center of the vessels is enhanced on all three planes of view, while if we
had adopted only a positive phase mask we would have produced a signal
decrease at the center of the vessels when viewing from the transverse plane,
and at the borders of the vessels when viewing from the coronal and sagittal

planes. This guarantees that the signal of the vessels is always decreased at
their center avoiding the overestimation of their diameter.



(a)



(b)



(c)
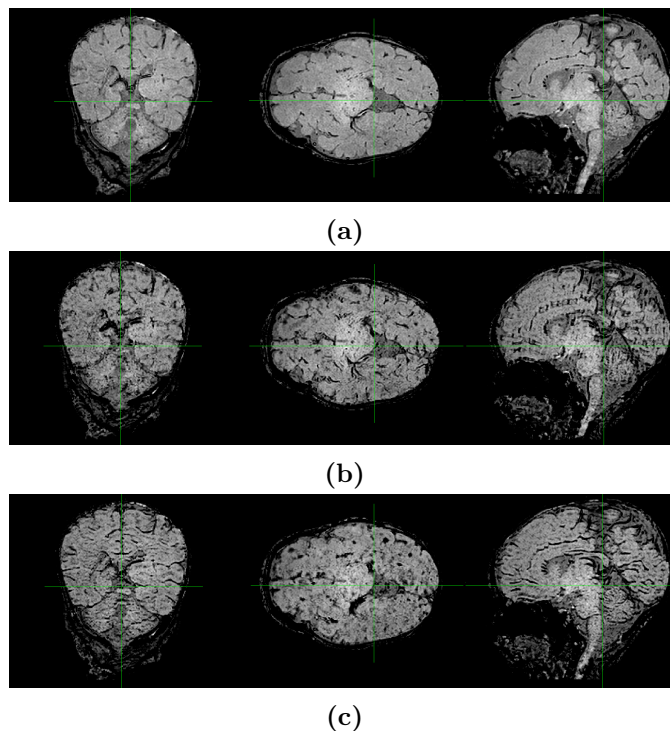
**Figure 3.13:** (a) Newborn magnitude image obtained with 1:1 voxel ratio. (b)
Newborn positive phase mask SWI with 1:1 voxel ratio. (c) Newborn negative
phase mask SWI with 1:1 voxel ratio.

## 3.6   Minimum Intensity Projection of 1:1 voxel ratio images

When acquiring images at 1:4 voxel ratio, because the voxel thickness is so
much bigger than the in-plane resolution, usually it is only useful to cre-
ate minimum intensity projections along the transverse plane. On the other
hand, when acquiring images at a 1:1 ratio it becomes reasonable to produce
minimum intensity projection images along the three different planes of view.

The GUI "Generate mIPs" button (recall Figure 3.9) was hence modified
in order to produce minimum intensity projections along the three planes of
view, and therefore, allowing us to obtain images such as shown in Figure
3.14.

**Figure 3.14:** Minimum intensity projection of a SWI of a newborn brain
acquired with a 1:1 voxel ratio.

These images allow the user to have a sense of how each vessel or structure relates to each other over the entire brain. This is of 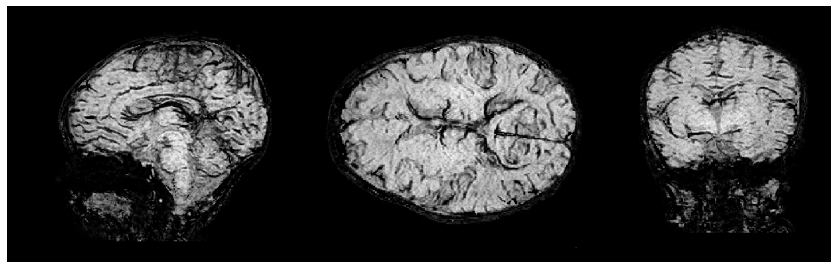special interest for depicting when small bleeds occurs inside the brain, because having a view over different three planes allows an easier differentiation of their shape and size.

## 3.7   Neonatal Brain SWI

Within this chapter it was discussed how it is possible to obtain a SWI neonatal protocol from the commonly used adult one. The main goal of this chapter was to implement a neonatal protocol that could be used in a clinical setting. In order to test and probe a satisfactory protocol, 13 volunteer babies with informed consent given by their parents where scanned on a Philips 3T Achieva scanner according to local ethical approval requirements. This way it was possible to test a range of repetition times between 28ms and 32ms as well as a range of FA between $10°$ and $14°$ in order to obtain a good compromise between acquisition time and signal to noise ratio. This allowed us, after visual inspection between different exams, to obtain the following protocol:

- 3D sagittal spoiled gradient echo sequence

- $T_E = 25$ ms

- $T_R = 32$ ms

- Flip Angle $= 12°$

- voxel size 0.65 mm $\times$0.65 mm $\times$0.65 mm

- SENSE factor $2.1 \times 2.1$

This set-up allows a full 3D image of the neonatal brain with an acquisition time below 5 minutes.

# Chapter 4

# DESPOT Versus Multi Component DESPOT

In this chapter the issue of how to correctly process a set of multi-angle SPGR and SSFP signals in order to estimate $T_1$ and $T_2$ maps is covered. We start be describing the implementation of a single component signal model and in section 4.1 we show how this can be used to generate test data with noise added that is then fitted with a suitable model to explore the precision and accuracy of the results. In section 4.2 this is extended to a 2 component model and an evaluation of its estimation precision and accuracy is performed. Having demonstrated some basic properties of the parameter estimation methods under 1 or 2 component scenarios, a systematic exploration of how to optimize DESPOT is presented in chapter 5.

Unless otherwise stated, along this chapter all simulations and processing steps were done in MatLab 2012a environment.

## 4.1 Estimation of $T_1$ and $T_2$

In order to produce a processing tool that correctly estimates $T_1$ and $T_2$ from a given data-set, a computer model of the one compartment expected signal behaviour inside a given voxel was generated. This allows us to have a data-set with known $T_1$ and $T_2$ parameters that can easily be tested under real-life settings.

The noise of magnitude MR images noise has been shown to follow the Rice distribution[31, 36] (Equation 4.1)

$$P(M) = \frac{M}{\sigma^2} I_0 \left( \frac{AM}{\sigma^2} \right) e^{\left( -\frac{A^2 + M^2}{2\sigma^2} \right)} \tag{4.1}$$

where, $M$ is the apparent measured signal, $A$ is the true signal, $\sigma$ is the standard deviation of the noise added to both the real and imaginary parts of the MR signal (which we assume to be the same) and $I_i$, $i = 0, 1, 2, 3, ...,$ are the modified Bessel functions of the first kind.

In order to generate SPGR and SSFP signals with Rician noise, normal distributed noise $\mathcal{N}(0, \sigma)$ was added to both the real and imaginary parts of the signals. Following the notation presented in section 2.3 we defined our noisy model as:

$$S_{SPGR}^{noisy} = |(SPGR + i0) + (\mathcal{N}(0, \sigma) + i\mathcal{N}(0, \sigma))| \qquad (4.2)$$

$$S_{SSFP}^{noisy} = |(M_x^{SS} + iM_y^{SS}) + (\mathcal{N}(0, \sigma) + i\mathcal{N}(0, \sigma))| \qquad (4.3)$$
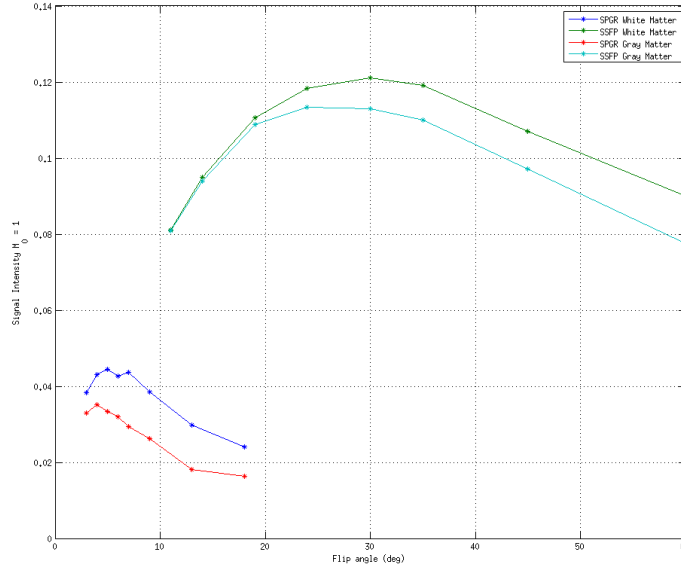


**Figure 4.1:** Example of a simulated DESPOT data-set for both white matter (dark blue and green curves) and gray matter (red and light blue curves). This set of signals was generated considering $M_0 = 1$ arbitrary unit and with an added noise of $\sigma = 1 \times 10^{-3}$.

Recalling from section 2.3 that DESOPT1 and DESPOT2 consist of estimating $T_1$ and $T_2$ from a set of signal measurements over different flip angles, it is possible to use Equations 4.2 and 4.3 to simulate this experiment and create model fitting routines.

Based on the work presented by Stanisz et al. in 2005 [37] two sets of tissue relaxation times were considered in an adult brain: White matter (WM) with a $T_1 = 1084$ ms and a $T_2 = 69$ ms, and Gray matter (GM) with a $T_1 = 1820$ ms and a $T_2 = 99$ ms. Assuming a repetition time of $T_R = 4.36$ ms for the SPGR signal and $T_R = 4.567$ ms (minimum $T_R$ times allowed by the scanner) for the SSFP signal and a set of flip angles such that $\theta_{SPGR} = (3°, 4°, 5°, 6°, 7°, 9°, 13°, 18°)$ and $\theta_{SSFP} = (10°, 13°, 17°, 20°, 23°, 30°, 43°, 60°)$[30], for an added noise of $\sigma = 1 \times 10^{-3}$ with an assumed $M_0 = 1$ it is possible to obtain the signal curves presented in Figure 4.1, which represent the signal variation of the SPGR and SSFP curves for both white matter and gray matter (respectively dark blue, green, red and light blue curves) over different flip angles.
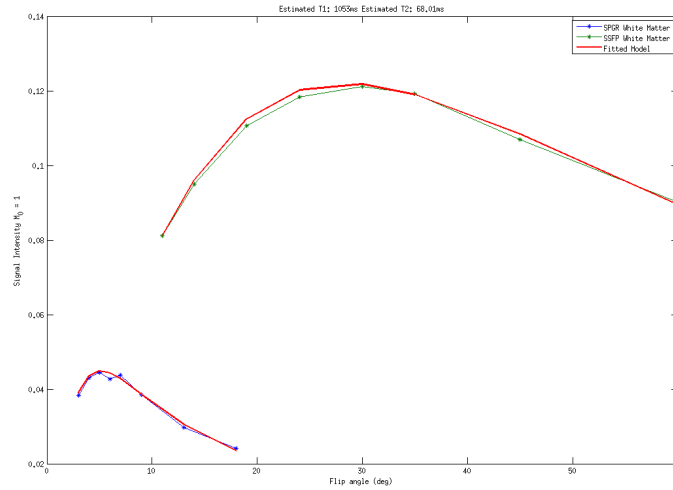


**Figure 4.2:** This figure shows the obtained fitted model (red curves) obtained using the MatLab2012a *fminsearch tool* superimposed over the original noisy SPGR (dark blue) and SSFP (green) data. The estimated parameters are $T_1 = 1053$ms and $T_2 = 68$ms which are close to simulated white matter values.

To derive the estimates of $T_1$ and $T_2$ parameters used to generate the signals presented in Figure 4.1 a fit of the SPGR and SSFP models was performed using MatLab2012a's "simplex" algorithm implemented as *fminsearch tool*. The cost function was defined as the minimization between the difference of the model and the data, and the stopping criteria was set as $1 \times 10^{-6}$ of the obtained solution or to a maximum number of iterations of $200 \times Number\ of\ variables$. Applying this to the white matter data shown in Figure 4.1 we were able to obtain the fitted model presented in Figure 4.2.

(a)           (b)

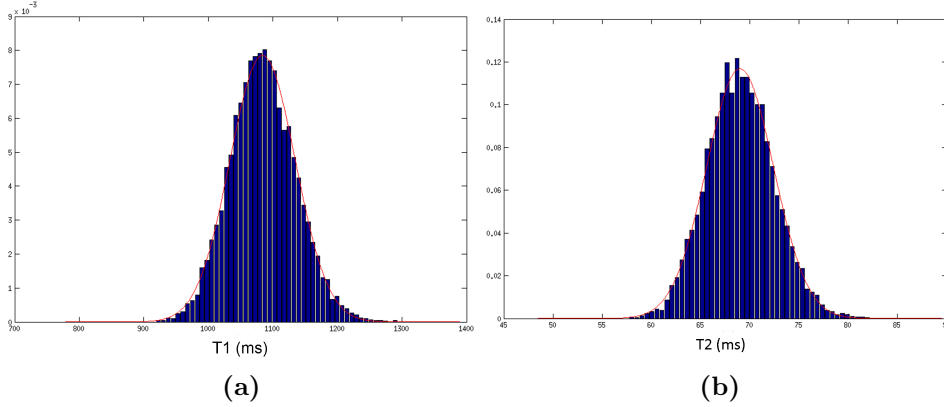**Figure 4.3:** (a) DESPOT estimation of $T_1$ histogram, $\mu \pm \sigma = 1083 \pm 51$ms. (b) DESPOT estimation of $T_2$ histogram, $\mu \pm \sigma = 69 \pm 3$ms. The obtained $\mu$ and $\sigma$ values were obtained by fitting the histogram to a Rice distribution.

The obtained estimated parameters in the case presented in Figure 4.2 were $T_1 = 1053$ms and $T_2 = 68$ms which represents a $T_1$ deviation of 2.9% and a $T_2$ deviation of 1.4. One obvious question that arises is how does this fitting procedure behave over a large number of noisy tests. In order to answer this question Monte Carlo simulation were done where 10000 noisy sets where simulated and fitted. The estimated parameters histograms can be seen in Figure 4.3.

The histograms presented in Figure 4.3 represent more clearly the accuracy and precision of the fitting procedure. If we define the variation coefficient as $p = \sigma/true\ value$ then we can see that when estimating $T_1$ we obtain $p = 0.047$ and for $T_2$ we obtain $p = 0.050$, which indicates a good estimation precision for this method.

So far we have assumed that the SSFP signal was on resonance (offset frequency band with high signal - recall Figure 2.5), however, in general there is a frequency offset variation along the human brain and this factor needs to be taken into account. One way to overcome this issue is to produce two sets of SSFP curves and making sure that they have a frequency offset shift of $\pi$, this allows a third parameter to be estimated which tells us in which frequency position of the graph presented in Figure 2.5 we are.

With this extra parameter to fit the problem dimensionality rises to three unknown parameters, however we found that the *"simplex" fminsearch tool* still allows an easy and precise convergence towards the right solutions, we were therefore able to try this set-up in a healthy volunteer and obtain the $T_1$, $T_2$ and frequency offset ($\psi$) maps shown in Figure 4.4. This data was

**(a)**



**(b)**



**(c)**
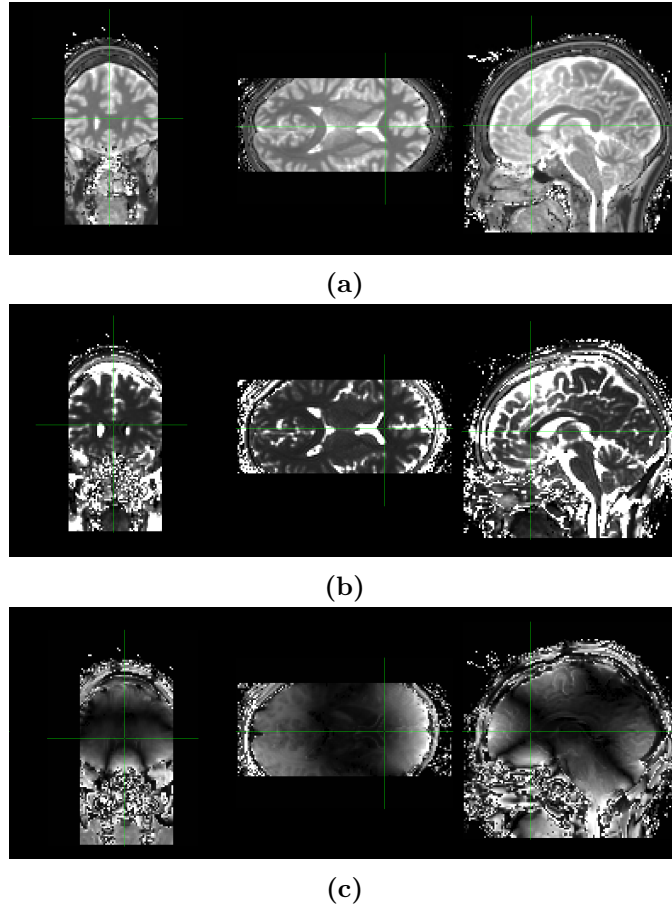
**Figure 4.4:** Maps obtained from fitting one-pool DESPOT model to data obtained from a healthy volunteer.(a) $T_1$ map. (b) $T_2$ map. (c) $\psi$ map. The selected point represented by the centre of both green lines has a $T_1 = 1023$ms, $T_2 = 39$ms and a $\psi = 0.9$rad

obtained on a Phillips 3T Achieva scanner and informed consent was given according to local ethic approval procedures.

In this discussion $M_0$ is ignored because before fitting all signals are divided by their respective mean value, in order to avoid fitting for $M_0$.[27, 30]

The set of images used to create the maps presented in Figure 4.4 were acquired over the sagittal plane with a resolution of 1.8mm×1.8mm×1.8mm, and a SENSE factor of 1.5 × 1.5 over the Right-Left and Anterior-Posterior directions.

## 4.2 Evaluation of mcDESPOT model

In the previous section the precision of the single component DESPOT model to estimate $T_1$ and $T_2$ was evaluated. In this section we evaluate the precision of the two-pool model proposed by Deoni et al. in 2008 [27].



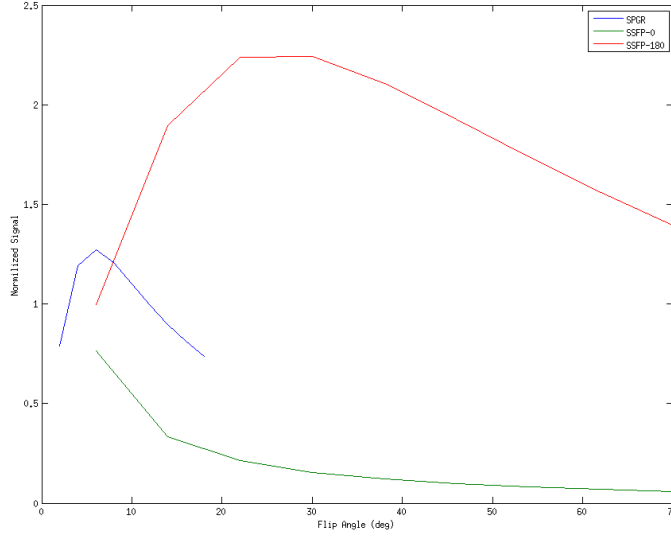**Figure 4.5:** This figure represents the normalized SPGR (dark blue), SSFP-$0°, 180°$ (red) and SSFP-$0°$ (green). The set of parameters used to generate these signals was: $T_{1,F} = 465$ms, $T_{1,S} = 1070$ms, $f_F = 0.2$, $\tau_{F,S} = 100$ms$^{-1}$, $T_{2,F} = 26$ms, $T_{2,S} = 117$ms, $\psi = 0$rad

As done in the previous section we start by implementing a two-pool signal model over different flip angles with added normal distribution noise to both the real and imaginary parts of the signals in order to obtain a Rice distribution after calculating the image magnitude. This two-pool model expands the problem dimensionality from three unknown parameters to seven unknown parameters, making the fitting procedure much harder and requires more creative approaches to obtain the correct estimation of parameters.

We first start by simulating the two-pool model. For reproducibility reasons we chose the set of parameters presented by Deoni et al. in their 2008 paper [27]. After this, the SPGR and the SSFP signals are normalized relative to their respective mean value (the SSFP-$0°$ and SSFP-$0°, 180°$ were considered coupled and the mean signal over all SSFP flip angles was considered in order to reduced noise scaling - Figure 4.5). This is done in order to avoid fitting for $M_0$ and reduce the dimensionality of the problem.

For the two-pool model we found that the "simplex" fitting procedure no longer converged to a solution with the desired accuracy and precision. To overcome this issue a more creative approach was designed in order to guarantee a correct estimation. When running optimization routines on non-linear search spaces, the starting point is a crucial factor towards finding a correct solution. In order to make sure the best solution was obtained a dictionary was generated over a grid of physiologically meaningful relaxation parameters. Using an orthogonal matching pursuit approach [38, 39] we were able to select of parameters that best explain the collected data. This set of starting point candidates where then rank-ordered by a least-squares criteria, and the best 100 candidates were used as starting points for a non-linear least-squares optimization, MatLab 2012a routine *lsqnonlin tool*. We then picked the rank-ordered obtained solutions by a least-squares difference criteria in order to select the solution that better explained the data as the correct one.



**Figure 4.6:** Example of the obtained fit solution (red) plotted against the simulated SPGR (green), SSFP-0° (dark blue)and SSFP-0°, 180° (black). The correct solution is also shown in light blue. The obtained solution is: $T_{1,F} = 465$ms, $T_{1,S} = 1070$ms, $f_F = 0.20$, $\tau_{F,S} = 100$ms, $T_{2,F} = 26$ms, $T_{2,S} = 117$ms and $\psi = 1.6 \times 10^{-6}$rad.

In order to test this fitting procedure we first applied it to a practically noiseless case (added $\sigma = 1 \times 10^{-7}$) and we realised that the fitting procedure

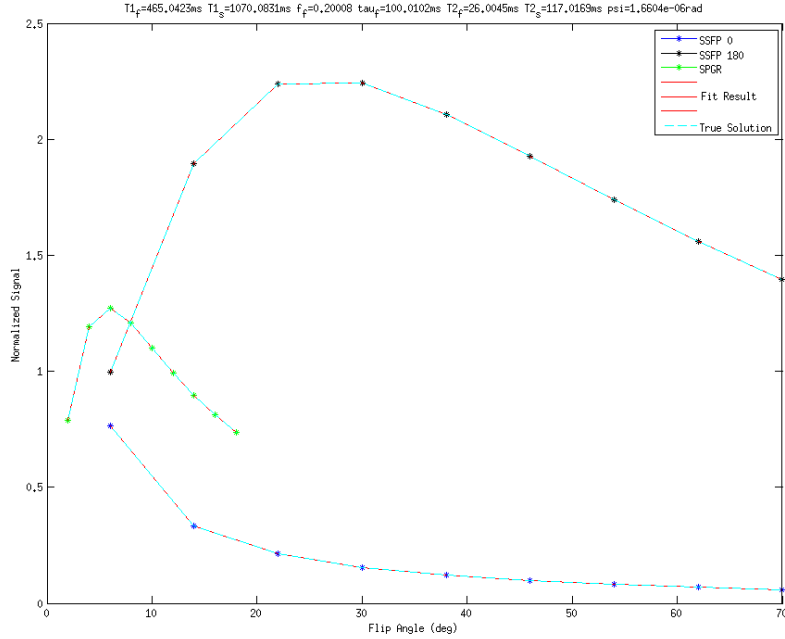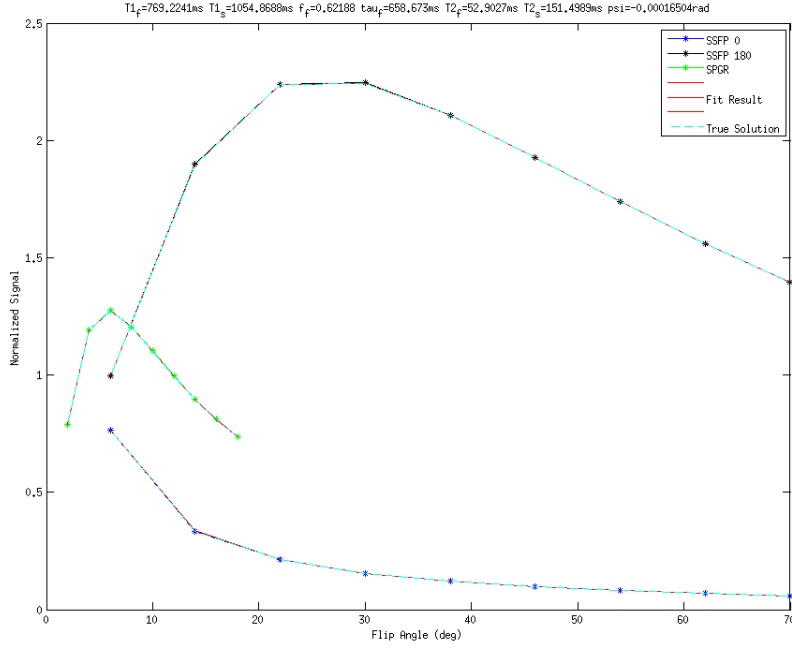was able to find the correct solution (Figure 4.6).



**Figure 4.7:** Example of the obtained fit solution (red) plotted against the simulated SPGR (green), SSFP-0° (dark blue) and SSFP-0°, 180° (black). The correct solution is also show in light blue. The obtained solution is: $T_{1,F} = 769$ms, $T_{1,S} = 1055$ms, $f_F = 0.62$, $\tau_{F,S} = 659$ms, $T_{2,F} = 53$ms, $T_{2,S} = 151$ms and $\psi = -0.0002$rad.

The next step was to try and apply this same procedure to a data-set with a small amount of noise added ($\sigma = 1 \times 10^{-4}$). Figure 4.7 shows the result for that fitting procedure. As can be seen the correct answer was no longer found, however what is very concerning is that the curves of the fitted model, and of the correct model are practically overlapping. In order to assess this, it was decided to try and visualize how the cost-function search space behaves along a straight line that connects the 100 best found solutions and the correct answer. The results are shown in Figure 4.8 and it is astonishing to see that no significant differences seen between the found solutions and the correct solution.

Looking carefully at Figure 4.8 it can be seen that the found solutions give a lower cost-function value than the correct answer, which suggests that this is an intrinsic problem of the model and not of the way we are searching for the correct parameter estimates.

These results agree with what is discussed in the paper published by
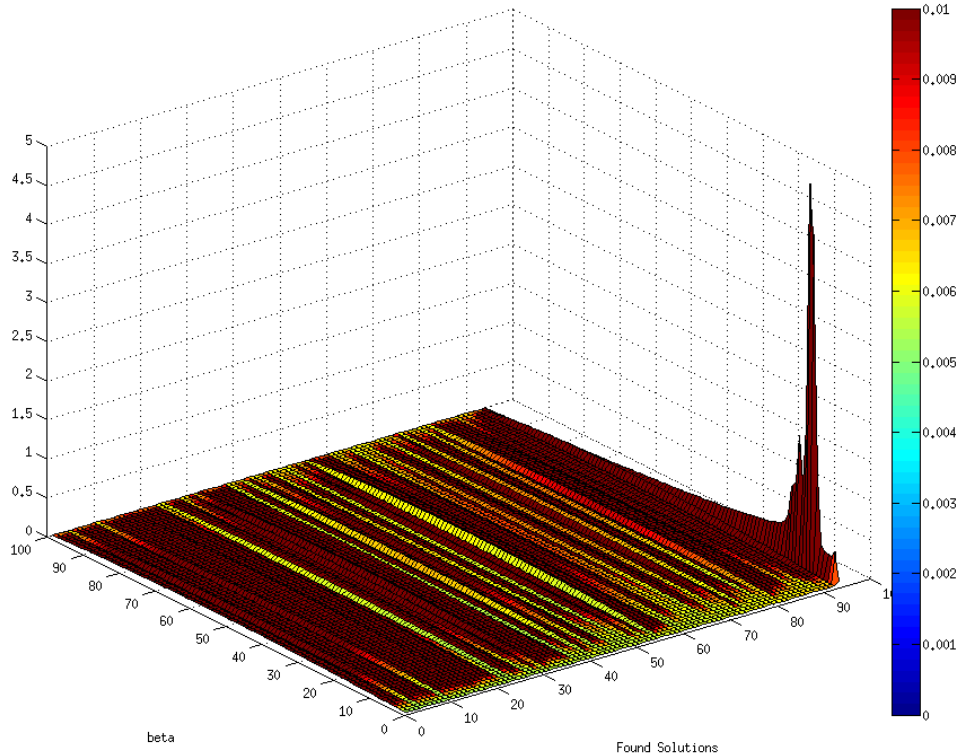
**Figure 4.8:** Representation of the mcDESPOT search-space topography along lines between the 100 best found solutions ($\beta = 0$) and the correct answer ($\beta = 100$). The found solutions are ordered from the best found solution (left) to the worse found solution (right). The color-bar represents the cost-function values scaled from the lowest obtained value to the highest.

Christopher L. Lankford and Mark D. Does in 2013 [31]. This paper suggests that mcDESPOT-derived estimates of tissue parameters do not have enough precision to be related to specific tissue characteristics. Their results indicate that previously published results, may have used data fitting methods that implicitly constrained parameter solution, or that the two-pool model may not be sufficient to describe the observed SPGR and SSFP signals.

In 2012 Deoni et al. proposed a three-pool mcDESPOT model, stating that it should be able to more precisely estimate water-pool parameters, however it was decided that this approach would make the fitting procedure even more difficult and was not relevant to follow this even more complex model line of thought within the scope of this work. Rather, it was decided to implement a framework to explore systematically a set of flip angles that guarantee a low estimation variance over different tissue parameters.

# Chapter 5

# Optimizing DESPOT

In the previous chapter it was discussed how to implement the standard DESPOT and mcDESPOT protocol and an assessment was done of the accuracy and precision of both methods.

In their 2013 paper[31], Christopher L. Lankford and Mark D. Does, used a statistical tool known as the Cramér-Rao Lower bound (CRLB) as a way to predict the minimum possible variance one can obtain when estimating parameters using the mcDESPOT two-pool model. The CRLB has been used in previous work as an optimization tool for MR protocols[36, 40, 41]. In this chapter we adapted this statistical tool to both verify and optimize the DESPOT protocol precision and accuracy.

One important question that arises is how can the CRLB be computed and once this is done, how can we use it as an optimization tool for our protocol? These are the main issues which are discussed in the following sections.

## 5.1 Cramér-Rao Lower Bound - Gaussian noise

The most common way to derive the CRLB is assuming a Gaussian distributed noise level[31, 36]. Following the notation presented in [31], if we assume a model $g(x, \theta)$, where $x \in \Re^N$ is an independent parameter vector (for what this work is concerned the flip angles) and $\theta \in \Re^M$ is a vector of model parameters ($T_1$ and $T_2$). Considering a set of $N$ noisy observations $y \in \Re^N$ from which we obtain a random estimate $\widehat{\theta}$, the estimated parameter vector covariance matrix is bounded by:

$$\Sigma_{\widehat{\theta}} \geq \frac{\partial E[\widehat{\theta}]}{\partial \theta} F^{-1} \frac{\partial E[\widehat{\theta}]}{\partial \theta}^T \tag{5.1}$$

where, $F$ is the Fisher information matrix (FIM), $E[.]$ is the expectation operator, and the derivative of one vector with respect to another follows the convention $(\partial a/\partial b)_{ij} \equiv \partial a_i/\partial b_j$.

The FIM is a matrix built from the parameter vector $\theta$ log-likelihood hyper-surface ($L$) curvature[31]. Which in the case of Gaussian distributed noise of the observed data $y_i, i = 1, 2, 3, ..., N$ simplifies into [31, 36, 42]:

$$F_{jk} = E(\frac{\partial^2 L}{\partial \theta_j \partial \theta_k}) = \sum_{i=1}^{N}(\frac{1}{\sigma_i^2}\frac{\partial g_i}{\partial \theta_j}\frac{\partial g_i}{\partial \theta_k}) \qquad (5.2)$$

In Equation 5.1 the CRLB also includes the estimator gradient matrix, however for unbiased estimators this term reduces to an identity matrix. Unless stated otherwise, along this work this unbiased condition is considered true and therefore $\partial E[\widehat{\theta}]/\partial \theta$ is considered to be the identity matrix.

Because all signals are considered to be magnitude signals, and we add Gaussian distributed noise to both the real and imaginary signal components, the resulting measured signal noise follows a Rician distribution. This means that the Gaussian CRLB model is only valid for signals with intensities at least two times bigger than the noise floor [31], therefore we found instructive to estimate the CRLB assuming also a Rice distribution of the noise model. A small overview of how this is achieved is discussed in the next section.

## 5.2 Cramér-Rao Lower Bound - Rician noise

The Rice distribution follows the distribution shown in equation 4.1. The log-likelihood of a set of $N$ measurements can therefore be expressed as:

$$L = \sum_{i=1}^{N}[\log M_i - 2\log \sigma + \log I_0(\frac{A_i M_i}{\sigma^2}) - \frac{A_i^2 + M_i^2}{2\sigma^2}] \qquad (5.3)$$

With this in mind the FIM may be computed by:

$$F_{jk} = E(\frac{\partial^2 L}{\partial \theta_j \partial \theta_k}) = \int_0^{\infty} \frac{\partial^2 L}{\partial \theta_j \partial \theta_k} P(M) dM \qquad (5.4)$$

which according to [36] can be expressed as:

$$E(\frac{\partial^2 L}{\partial \theta_j \partial \theta_k}) = \sum_{i=1}^{N} \frac{1}{\sigma^4}\frac{\partial A_i}{\partial \theta_j}\frac{\partial A_i}{\partial \theta_k}(Z_k - A_k^2) \qquad (5.5)$$

where,

$$Z_k = \int_0^\infty A_i^2 I_1^2(\frac{A_i M}{\sigma^2}) I_0^{-2}(\frac{A_i M}{\sigma^2}) P(M) dM \qquad (5.6)$$

The function $Z_k$ must be numerically computed, since it does not have a closed form. Also, as suggested in [36], a look-up table was pre-computed and linear interpolation was used to assess $Z_k$ values in order to save computing time and resources.

## 5.3 Selection of optimized Flip Angle set

The main goal of the work presented in this chapter is to optimize the DESPOT protocol by selecting in a rigorous way the combination of flip angles that allow us to obtain the lowest estimation variance possible.

### 5.3.1 Defining Cost Function

In order to find a set of $N$ flip angles that minimizes the predicted CRLB and at the same time ensure that the relative precision of each parameter $(T_1, T_2)$ is equally weighted, we normalize the CRLB of each parameter by its respective squared value. As the brain has a heterogeneous range of $T_1$ and $T_2$ values that we wish to optimize for. We consider a cost function that computes the CRLB over a $T_1$ and $T_2$ grid and selects the combination of parameters that gives the highest CRLB. Minimizing the output of this cost function guarantees the optimization of the worst case scenario in each step of the optimization procedure[42].

### 5.3.2 Simulated Annealing

Simulated annealing is an optimization routine that is known to be suitable for large scale problems, since it doesn't rely on gradient estimation to find a global minimum solution.

This method is inspired on thermodynamics, more specifically on how metals cool and anneal, or liquids freeze and crystallize. At high temperatures, the liquid molecules are able to freely move with respect to each other, however when the temperature drops slowly, this mobility is lost. During this process the atoms are able to line themselves and form a pure crystal (lowest energy state). Mimicking this natural process is the heart of simulated annealing. This process can be modelled by the Boltzmann distribution,

$$P(E) \sim e^{-E/kT} \qquad (5.7)$$

which describes the idea that a system in thermal equilibrium at a temperature $T$ has a probability to be distributed over different energy states $E$. This allows the systems to leave low energy states (local minima) in favour of finding better ones (global minima)[43].

This optimization routine is implemented in MatLab2012a optimization toolbox *optimtool*, and was used to evaluate the previously discussed cost function in order to find a set of flip angles that allow low $T_1$ and $T_2$ estimation variances.

### 5.3.3 Verifying the CRLB

One important first step is to verify if the predicted bound agrees with the fitting procedure implemented. A Monte Carlo simulation was performed in order to compare the predicted bound with the obtained fit standard deviation over a large number of trials.

The Rice distribution is known to converge towards a Gaussian distribution for $SNR > 3$ [44], and therefore for simplicity we assumed the Gaussian distributed CRLB. Because this model does not assume the data is normalized prior to the fitting procedure, in order to maintain equity between obtained standard deviation and predicted CRLB, the data was fitted without the normalization step, and $M_0$ was considered as an extra parameter.

The Monte Carlo simulation was set-up as followed: 10000 noisy SPGR and SSFP-$0°, 180°$ trails were generated. Correct knowledge of $\psi$ was considered since it can be assessed with $B_0$ mapping techniques. The considered parameters were $\sigma = 1 \times 10^{-3}$, $M_0 = 1$, $T_1 = 1083$ms and $T_2 = 69$ms. The simulated data was fitted using *fminsearch tool* for $M_0$, $T_1$ and $T_2$ parameters using the correct answer as the starting point. The obtained histograms and predicted CRLB can be seen in Figure 5.1. This Figure shows that the CRLB and the obtained histograms standard deviation are in excellent agreement and therefore the CRLB can be used as a means to predict the parameter estimation error given a set of parameters.

Once this was verified, the CRLB was used to select an optimized set of FA that would give a good compromise between parameter estimation error and acquisition time. Using the approach described in section 5.3.1 a grid of expected WM and GM parameters expected in the neonatal brain was considered. $T_{1,WM} \cup T_{1,GM} = [2300; 2700] \cup [1600; 2000]$ms in increments of 50ms and $T_{2,WM} \cup T_{2,GM} = [20; 200]$ms in increments of 20ms [35]. The optimization was performed for sets of 16, 14, 12, 10, 8, 6, and 4 FA. Each set had equal number of SPGR and SSFP measurements. The optimized
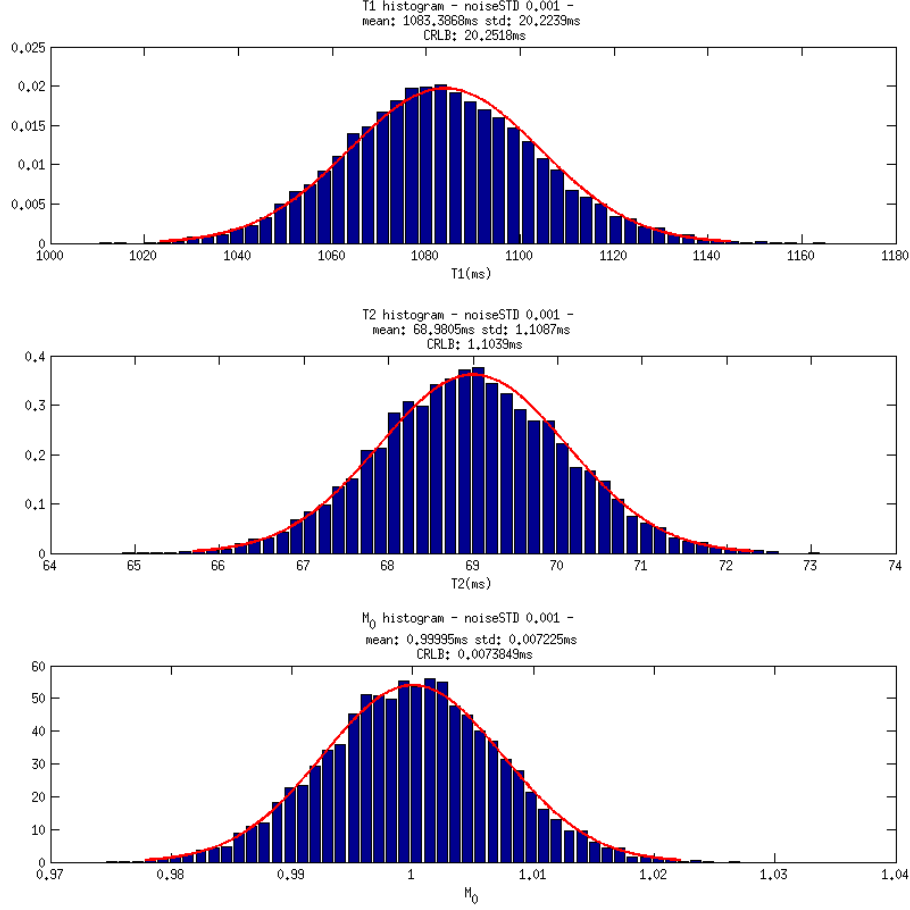
**Figure 5.1:** This Figure show the CRLB predicted distribution (red) versus the obtained histograms from the Monte Carlo simulations (blue), for $T_1$ (top), $T_2$ (middle) and $M_0$ (bottom).

set of 16 FA is:

- SPGR:$4.60°, 5.32°, 5.51°, 5.86°, 6.14°, 6.88°, 9.93°, 21.47°$

- SSFP:$6.67°, 14.97°, 16.24°, 20.12°, 22.80°, 23.70°, 33.63°, 84.87°$

In order to compare the optimized FA with the original set, the predicted precision ($CRLB/TrueValue$) for both $T_1$ and $T_2$ was plotted over a grid of relaxation times (Figure 5.2). It can be seen that the optimized FA guarantee a lower CRLB over the range of relaxation times when compared with the original set. Looking more carefully at the obtained set of FA it is striking to see some of them are very close together, perhaps suggesting that the actual number of measurements can be reduced without strongly affecting the estimation precision. In fact, performing the optimization with only 2 SPGR (optimized to:$5.7°$ and $7.3°$) and 3 SSFP (optimized to:$14.3°, 24.0°$

47

and 60.0°) measurements still allows a predicted precision bellow 10% (Figure 5.3).
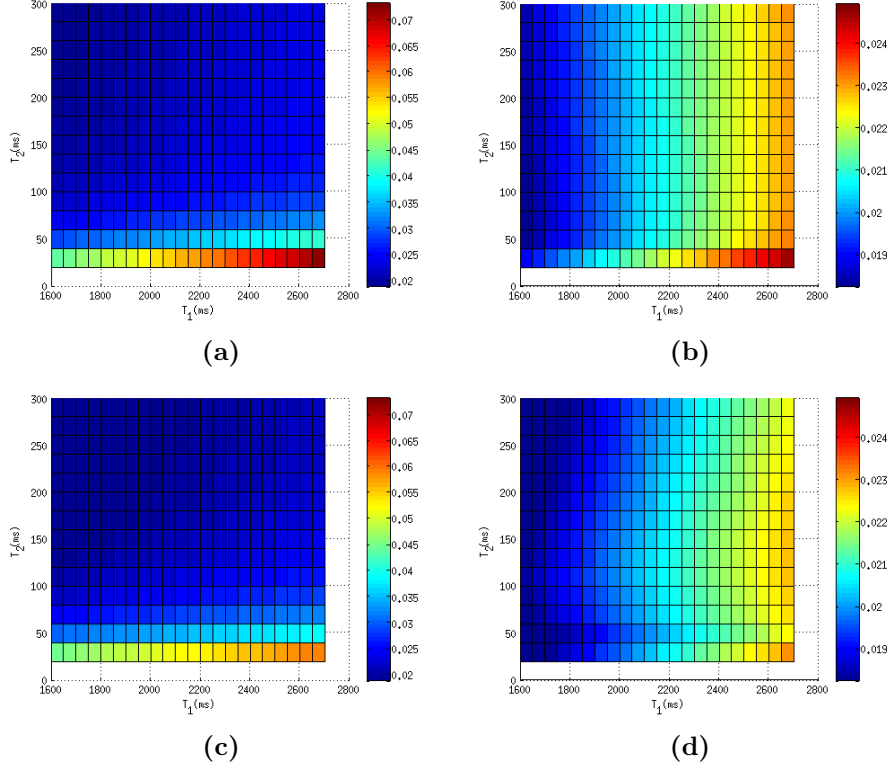


**Figure 5.2:** This figure shows how the estimated precision (precision $p = \sigma^2/T_{1,2}^2$, where red represents worse precision and dark blue best brecision obtained over the grid) and $T_2$((b) and (d)) changes over a grid of $T_1$ and $T_2$ parameters ranging from 1600ms to 2800ms (horizontal axis) and 20ms to 300ms (vertical axis) respectively. (a)(b) Gold-standard set-up. (c)(d) Optimized set-up.

Figure 5.3 shows that even with only 5 FA the model only has estimation errors larger than 10% for very high $T_1$ and low $T_2$ parameters.

The results shown so far indicate that the DESPOT1 and DESPOT2 set-up can be optimized using the CRLB. Picking the correct set of FA allows estimation of $T_1$ and $T_2$ parameters with an error bellow 10% with only 2 SPGR and 2 SSFP measurements.

It must be noticed that this optimization set-up is too simplistic, as in a clinical scanner the MR system performs internal receive and transmit calibrations at the beginning of each acquisition sequence resulting in different gain factors that may corrupt the estimation and should be taken

(a)                                        (b)
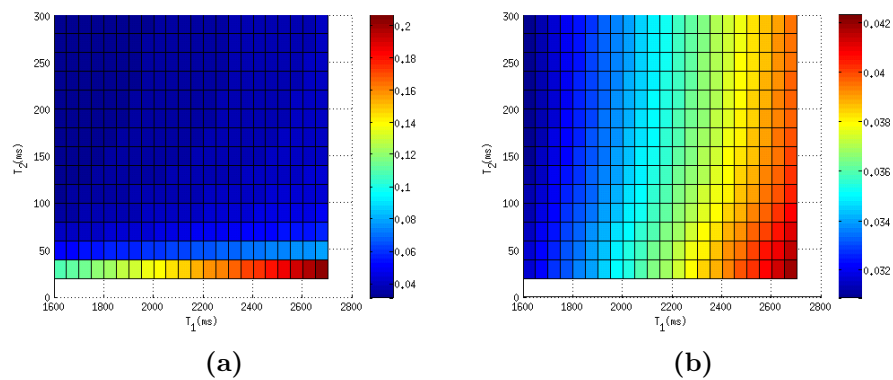
**Figure 5.3:** (a) $T_1$ and (b) $T_2$ estimation precision (precision $p = \sigma^2/T_{1,2}^2$, where red represents worse precision and dark blue best brecision obtained over the grid) with two SPGR flip angles (5.7° and 7.5°) and three SSFP (14.3°, 24.0° and 60.0°) over a grid of $T_1$(horizontal axis) and $T_2$ (vertical axis) parameters.

into account. This issue is usually overcome by normalizing the data by its respective mean, therefore one way to further improve this work would be to develop and implement a normalized signal CRLB model.

49

# Chapter 6

# Summary and Conclusion

This work has described how to apply advance MR techniques to image the neonatal brain.

In Chapter 3 it was discussed how to adapt standard adult SWI protocol to the neonatal brain. The goal was to create a SWI capability for use on neonatal brain. This involved proposing a dedicated neonatal protocol, including a re-evaluation of the effect of varying slice thickness and developing a GUI to allow users to produce filtered images that emphasise susceptibility effects from raw SWI data. The developed GUI will allow future systematic clinical testing and further explore some of the issues intrinsic to this type of MR imaging. Also we demonstrated that voxel size plays a very important role when SWI is concerned and that for isotropic ratios it should be taken into account not only positive phase information but also negative phase information. This however was not systematically evaluated and should be explored in future work.

Within Chapter 4 it was described how to correctly process a set of multi-angle SPGR and SSFP signals in order to estimate $T_1$ and $T_2$ for both a one compartment and two compartment models. We concluded that the single pool model can correctly estimate parameters with a precision around 5%. We were not able to obtain satisfying results from the two-pool model approach and decided that further work on the topic would not be important for the scope of this project.

In Chapter 5 the use of the CRLB as an optimization tool for DESPOT was discussed. Along this chapter we showed that the CRLB is in good agreement with the obtained estimation standard deviation from Monte Carlo simulations. Further we showed that it can be used to optimize the DESPOT acquisition protocol for a range of $T_1$ and $T_2$ parameters. We also concluded that it is possible to greatly reduce the number of FA samples

without significantly affecting the estimation of $T_1$ and $T_2$ precision.

In the end of this project both SWI and DESPOT, have been set-up with technical testing that provides the basis for full scale tests of the methods on neonatal subjects.

# Bibliography

[1] E. Mark Haacke, S. Mittal, Z. Wu, J. Neelavalli, and Yu-Chung N. Cheng. Susceptibility-weighted imaging: Technical aspects and clinical applications, part 1. *American Journal of Neuroradiology*, 30:19–30, January 2009.

[2] Reshiana Rumzan, Jing-jie Wang, Chun Zeng, Xuan Chen, Yongmei Li, Tianyou Luo, Fajin Lv, Zhong-ping Wang, Huanxin Hou, and Fuhong Huang. Iron deposition in the precentral grey matter in patients with multiple sclerosis: A quantitative study using susceptibility-weighted imaging. *European Journal of Radiology*.

[3] Chi S. Zee and Chenyu Yan. Susceptibility-weighted imaging at ultra-high field (7 t) in the evaluation of brain tumors. *World Neurosurgery*, 77(5–6):654–656, May 2012.

[4] Hagen H. Kitzler, Jason Su, Michael Zeineh, Cynthia Harper-Little, Andrew Leung, Marcelo Kremenchutzky, Sean C. Deoni, and Brian K. Rutt. Deficient MWF mapping in multiple sclerosis using 3D whole-brain multi-component relaxation MRI. *NeuroImage*, 59(3):2670–2677, February 2012.

[5] E. Mark Haacke, Robert W. Brown, Michael R. Thompson, and Ramesh Venkatesan. *Magnetic Resonance Imaging: Physical Principles and Sequence Design*. Wiley, June 1999.

[6] Jian-Ming Jin. *Electromagnetic Analysis and Design in Magnetic Resonance Imaging*. Crc Press, 1999.

[7] Donald W. McRobbie, Elizabeth A. Moore, Martin J. Graves, and Martin R. Prince. *MRI from Picture to Proton*. Cambridge University Press, 2 edition, February 2007.

[8] Matt A. Bernstein, Kevin Franklin King, and Xiaohong Joe Zhou. *Handbook of MRI Pulse Sequences*. Elsevier, September 2004.

[9] John Homer and Martin S Beevers. Driven-equilibrium single-pulse observation of t1 relaxation. a reevaluation of a rapid "new" method

for determining NMR spin-lattice relaxation times. *Journal of Magnetic Resonance (1969)*, 63(2):287–297, June 1985.

[10] Sean C.L. Deoni, Brian K. Rutt, and Terry M. Peters. Rapid combined t1 and t2 mapping using gradient recalled acquisition in the steady state. *Magnetic Resonance in Medicine*, 49(3):515–526, 2003.

[11] Richard G.S Spencer and Kenneth W Fishbein. Measurement of Spin–Lattice relaxation times and concentrations in systems with chemical exchange using the one-pulse sequence: Breakdown of the ernst model for partial saturation in nuclear magnetic resonance spectroscopy. *Journal of Magnetic Resonance*, 142(1):120–135, January 2000.

[12] Klaus Scheffler. A pictorial description of steady-states in rapid magnetic resonance imaging. *Concepts in Magnetic Resonance*, 11(5):291–304, 1999.

[13] Klaus Scheffler and Stefan Lehnhardt. Principles and applications of balanced SSFP techniques. *European Radiology*, 13(11):2409–2418, November 2003.

[14] Sergio Casciaro, Roberto Bianco, Roberto Franchini, Ernesto Casciaro, and Francesco Conversano. A new automatic phase mask filter for high-resolution brain venography at 3 t: theoretical background and experimental validation. *Magnetic Resonance Imaging*, 28(4):511–519, 2010.

[15] Zhen Wu, Sandeep Mittal, Karl Kish, Yingjian Yu, J. Hu, and E. Mark Haacke. Identification of calcification with MRI using susceptibility-weighted imaging: A case study. *Journal of Magnetic Resonance Imaging*, 29(1):177–182, 2009.

[16] William M. Spees, Dmitriy A. Yablonskiy, Mark C. Oswood, and Joseph J.H. Ackerman. Water proton MR properties of human blood at 1.5 tesla: Magnetic susceptibility, t1, t2, t *2, and non-lorentzian signal behavior. *Magnetic Resonance in Medicine*, 45(4):533–542, 2001.

[17] Robert M. Weisskoff and Suzanne Kiihne. MRI susceptometry: Image-based measurement of absolute susceptibility of MR contrast agents and human blood. *Magnetic Resonance in Medicine*, 24(2):375–383, 1992.

[18] Yingbiao Xu and E. Mark Haacke. The role of voxel aspect ratio in determining apparent vascular phase behavior in susceptibility weighted imaging. *Magnetic Resonance Imaging*, 24(2):155–160, 2006.

[19] Y. Wang et al. Artery and vein separation using susceptibility- dependent phase in contrast-enhanced MRA. *Journal of Magnetic Resonance Imaging*, 12:661–670, May 2000.

[20] Valentina Brainovich, Umberto Sabatini, and Gisela E. Hagberg. Advantages of using multiple-echo image combination and asymmetric triangular phase masking in magnetic resonance venography at 3 t. *Magnetic Resonance Imaging*, 27(1):23–37, 2009.

[21] S. Ogawa, T. M. Lee, A. R. Kay, and D. W. Tank. Brain magnetic resonance imaging with contrast dependent on blood oxygenation. *Proceedings of the National Academy of Sciences*, 87(24):9868–9872, 1990.

[22] J. R. Reichenbach, R. Venkatesan, D. J. Schillinger, D. K. Kido, and E. M. Haacke. Small vessels in the human brain: MR venography with deoxyhemoglobin as an intrinsic contrast agent. *Radiology*, 204(1):272–7, July 1997.

[23] E. Mark Haacke, Yingbiao Xu, Yu-Chung N. Cheng, and Jurgen R. Reichenbach. Susceptibility weighted imaging (SWI). *Magnetic Resonance in Medicine*, 52(3):612–618, 2004.

[24] Andreas Deistung, Alexander Rauscher, Jan Sedlacik, Jörg Stadler, Stephan Witoszynskyj, and Jürgen R. Reichenbach. Susceptibility weighted imaging at ultra high magnetic field strengths: Theoretical considerations and experimental results. *Magnetic Resonance in Medicine*, 60(5):1155–1168, 2008.

[25] A S Hall, I R Young, F J Davies, et al. A dedicated magnetic resonance system in a neonatal intensive therapy unit. *Advanced MR Imaging Techniques*, pages 281–290, 1997.

[26] Tetsu Niwa, LindaS Vries, ManonJ N. L. Benders, Taro Takahara, PeterG J. Nikkels, and Floris Groenendaal. Punctate white matter lesions in infants: new insights using susceptibility-weighted imaging. *Neuroradiology*, 53(9):669–679, 2011.

[27] Sean C.L. Deoni, Brian K. Rutt, Tarunya Arun, Carlo Pierpaoli, and Derek K. Jones. Gleaning multicomponent t1 and t2 information from steady-state imaging data. *Magnetic Resonance in Medicine*, 60(6):1372–1387, 2008.

[28] Sean C.L. Deoni, Brian K. Rutt, and Derek K. Jones. Investigating exchange and multicomponent relaxation in fully-balanced steady-state free precession imaging. *Journal of Magnetic Resonance Imaging*, 27(6):1421–1429, 2008.

[29] Sean C.L. Deoni, Brian K. Rutt, and Derek K. Jones. Investigating the effect of exchange and multicomponent t1 relaxation on the short repetition time spoiled steady-state signal and the DESPOT1 t1 quantification method. *Journal of Magnetic Resonance Imaging*, 25(3):570–578, 2007.

[30] Sean C. L. Deoni, Lucy Matthews, and Shannon H. Kolind. One component? two components? three? the effect of including a nonexchanging "free" water component in multicomponent driven equilibrium single pulse observation of t1 and t2. *Magnetic Resonance in Medicine*, 2012.

[31] Christopher L. Lankford and Mark D. Does. On the inherent precision of mcDESPOT. *Magnetic Resonance in Medicine*, 69(1):127–136, 2013.

[32] A. Meoded, A. Poretti, F. J. Northington, A. Tekes, J. Intrapiromkul, and T. A. G. M. Huisman. Susceptibility weighted imaging of the neonatal brain. *Clin Radiol*, 67(8):793–801, August 2012.

[33] Miriam H. Beauchamp, Michael Ditchfield, Franz E. Babl, Michael Kean, Cathy Catroppa, Keith O. Yeates, and Vicki Anderson. Detecting traumatic brain lesions in children: CT versus MRI versus susceptibility weighted imaging (SWI). *Journal of Neurotrauma*, 28(6):915–927, June 2011.

[34] H. Uetani, T. Hirai, M. Hashimoto, M. Ikeda, M. Kitajima, F. Sakamoto, D. Utsunomiya, S. Oda, S. Sugiyama, J. Matsubara, and Y. Yamashita. Prevalence and topography of small hypointense foci suggesting microbleeds on 3T susceptibility-weighted imaging in various types of dementia. *American Journal of Neuroradiology*, 2012.

[35] Lori-Anne Williams, Neil Gelman, Paul A. Picot, David S. Lee, James R. Ewing, Victor K. Han, and R. Terry Thompson. Neonatal brain: Regional variability of in vivo MR imaging relaxation rates at 3.0 T—Initial experience1. *Radiology*, 235(2):595–603, May 2005. PMID: 15858099.

[36] Daniel C. Alexander. A general framework for experiment design in diffusion MRI and its application in measuring direct tissue-microstructure features. *Magnetic Resonance in Medicine*, 60(2):439–448, 2008.

[37] Greg J. Stanisz, Ewa E. Odrobina, Joseph Pun, Michael Escaravage, Simon J. Graham, Michael J. Bronskill, and R. Mark Henkelman. T1, t2 relaxation and magnetization transfer in tissue at 3T. *Magnetic Resonance in Medicine*, 54(3):507–512, 2005.

55

[38] J.A. Tropp and A.C. Gilbert. Signal recovery from random measurements via orthogonal matching pursuit. *IEEE Transactions on Information Theory*, 53(12):4655–4666, December 2007.

[39] Dan Ma, Vikas Gulani, Nicole Seiberlich, Kecheng Liu, Jeffrey L. Sunshine, Jeffrey L. Duerk, and Mark A. Griswold. Magnetic resonance fingerprinting. *Nature*, 495(7440):187–192, March 2013.

[40] Oscar Brihuega-Moreno, Frank P. Heese, and Laurance D. Hall. Optimization of diffusion measurements using cramer-rao lower bound theory and its application to articular cartilage. *Magnetic Resonance in Medicine*, 50(5):1069–1076, 2003.

[41] Angel R. Pineda, Scott B. Reeder, Zhifei Wen, and Norbert J. Pelc. Cramér–Rao bounds for three-point decomposition of water and fat. *Magnetic Resonance in Medicine*, 54(3):625–635, 2005.

[42] Mara Cercignani and Daniel C. Alexander. Optimal acquisition schemes for in vivo quantitative magnetization transfer MRI. *Magnetic Resonance in Medicine*, 56(4):803–810, 2006.

[43] Brian A. Teukolsky Saul T. Vetterling William H. Press, William P. Flannery. *Numerical Recipes*. Cambridge University Press, 1989.

[44] Hakon Gudbjartsson and Samuel Patz. The rician distribution of noisy MRI data. *Magnetic resonance in medicine : official journal of the Society of Magnetic Resonance in Medicine / Society of Magnetic Resonance in Medicine*, 34(6):910–914, December 1995. PMID: 8598820 PMCID: PMC2254141.